PEOPLE'S DEMOCRATIC REPUBLIC OF ALGERIA

MINISTRY OF HIGHER EDUCATION AND SCIENTIFIC RESEARCH

AMAR TELIDJI UNIVERSITY- LAGHOUAT

FACULTY OF TECHNOLOGY

Dissertation Master Degree in Microelectronic Engineering

Presented by: Mohammed BenAtallah

Design study of High-Efficiency Thermophotovoltaic Solar Vell

---

Board of Examiners:

Chairman:	**MAA**	**Aissa Bellakhdar**	**UATL**
Examiner:	**MAA**	**Younes Khadidja**	**UATL**
Supervisor:	**Prof**	**Ali Cheknane**	**UATL**
Co-supervisor:	**MCB**	**Fathi Bendelala**	**UATL**

2019/2020

ACKNOWLEDGEMENTS

First and foremost, all thanks and praise be to **Allah** the one who has helped me to finish this work. Over the course of my work, I was fortunate to be surrounded by family especially my father and my mother whose support and contribution were invaluable in both my academic and personal endeavors.

I would like to express my very great appreciation to **Dr. Fathi BENDELALA** for his valuable and constructive suggestions during the planning and development of this work, and I would like also to thank **Prof. Ali CHEKNANE** for giving me this opportunity to prove myself. His willingness to give his time so generously has been very much appreciated.

DEDICATIONS

This thesis is dedicated to my parents and my family and my unknown future wife for their unconditional love and never-ending support.

NOMENCLATURE

$A(\omega)$	Absorption
B	Magnetic flux density (T)
c	Speed of light in vacuum (m s^{-1})
CST	Computer simulation technology
D	Electric flux density or electric displacement ($C.m^{-2}$)
E	Electric field ($V.m^{-1}$)
E_g	Bandgap energy
EQE	External quantum efficiency
$\vec{E}$	Vector of Electric field
$e(\omega)$	the emittance of the metamaterial emitter
FF	fill factor
FEM	Finite element method
I_{SC}	short circuit current
I_{MPP}	Current of maximum Power Point
J_{ph}	photocurrent generated ($A\ m^{-2}$)
$\hbar$	Plank's constant ($6.62606957\times10^{-34} m.^2 kg.s^{-1}$)
H	Magnetic field ($A.m^{-1}$)
$\vec{H}$	Vector of Magnetic fild
HFSS	High frequency simulator system
IR	Infrared
k	Wave number
$\vec{k}$	wave vector
k_B	Boltzmann's constant ($1.3806\times10^{-23}\ J\cdot K^{-1}$)

MM	Metamaterial
n	Index of refraction
η_{TPV}	Thermophotoltaic cell efficiency
η_{diode}	diode efficiency
η_{sp}	spectral efficiency
P_{abs}	Absorbed power
P_{rad}	Radiated power
P_{out}	Output power
q	Charge of electron ($1.60217657 \times 10^{-19}$ C)
$\vec{S}$	Poynting vector
SRR	Split ring resonator
TPV	Thermophotovoltaic
TE	Transverse electric
TM	Transverse magnetic
TBB	Blackbody temperature
T_{BB}	Blackbody temperature
V_{oc}	open circuit voltage
V_{MPP}	Voltage of maximum Power Point
W	Tungsten
$Z_0(\omega)$	free space impedance
$Z_{eff}(\omega)$	impedance of MTM structure
$Z(\omega)$	Frequency dependent impedance
ω_p	Plasma frequency

ε_0	Permittivity free space (8.85 x 10-12 F/m)
Γ	Damping Constant
μ	Magnetic permeability
σ	Electric conductivity (s m^{-1})
χ_e	electric susceptibility
χ_m	magnetic susceptibility
λ_{gap}	Bandgap wavelength
$\varepsilon_{eff}(\omega)$	effective electric permittivity
$\mu_{eff}(\omega)$	effective magnetic permeability
ω	Angular frequency (Hz)
ε	Electric permittivity

Table of contents

List of figures

List of Tables

Abstract

Our manuscript studies the characteristics of a new design of selective Metamaterial (MM) emitter for near-infrared wavelength range, after a brief overview of MMs foundation, operating mechanisms with state of the art of TPV technologies. MM absorber/emitter for TPV application has been numerically investigated for a wide-band absorption with a selective emittance, this study highlights the theories, properties, and applications of MM absorber/emitter, and their requirements for an efficient conversion such as polarization-insensitive, wide-angle of incidence, thermal stability given by high melting temperature point of the used materials as SiO2 and Tungsten. A rigorous approach for simulation has been performed to understand the behavior of the new design at near-infrared and optical wavelength ranges, by using the HFSS solver based on the Finite Element Method (FEM). Absorption rates of 99% are numerically achieved covering a wide range from 120THz to 600THz. Finally, the suggested design has been exploited for the TPV system. The highest TPV conversion efficiency of 27% can be achieved by using two types of TPV cells (GaSb) and (InGaAsSb), for a high-temperature (2100°C), on the other hand, for low operating temperatures (e.g. T_{BB} = 600ºC), furthermore, (InAsSbP) TPV cell associates to achieve 22.5% of TPV conversion efficiency. Therefore, the selected absorber/emitter design can operate at a wide temperature range from 600 to 2100 ºC.

Keywords: *TPV cells (GaSb/* InGaAsSb */InAsSbP); thermophotovoltaic; selective emitter.*

ملخص

من خلال هذه الدراسة قمنا بطرح خصائص التصميم الجديد لباعث الانتقائي لنطاق الطول الموجي القريب من الأشعة تحت الحمراء بمواد تسمى المواد الغير طبيعيه,وهذا بعد القاء نظره عامه على اساسيات واليات والمبادئ النظريه للتحويل الضوئي الحراري وتسلط هذه الدراسه الضوء على نظريات الخصائص والتطبيقات للموارد الغير الطبيعيه ,كما يتمتع هذا الاخير بخصائص مختلف منها امتصاص واسع وامتصاص قابل لضبط حراريا و امتصاص منخفض للطاقة , وتم إجراء للمحاكاة بواسطة HFSS لفهم سلوك التصميم الجديد في نطاقات الأشعة القريبة من تحت الحمراء والتي تمت برمجتها بطرق معتمده ومختلفه منها طريقه العناصر المحددة و تم تحقيق معدلات امتصاص تصل بنسبة 99٪ عدديًا و تغطي نطاقًا واسعًا من 120 إلى 600 تيراهرتز في نسبات عالية للامتصاص والغير الحساس للاستقطاب, وبالتالي يمكن ان يعمل بفعاليه مقترنه بخلايا نظام تحويل الضوء الحراري لذلك قمنا باختيار ثلاث خلايا و تمت تجربتهن كلٌّ على حِدَة وبالمقارنه كانا (GaSb و InGaAsSb) قد حققا اعلى كفاءه لتحويل الضوئي بنسبه 27% لدرجه حراره عاليه كانت ما بين (1900 إلى 2100) درجه مئويه اما بالنسبه الى درجات الحراره المنخفضه والتي تصل الى 600 درجه مئويه فقد حققت (InAsSbP) اداء الرائع بحيث وصل كفاءه تحويل ضوئي الى 21% مقارنه بالخليتين السابقتين ,وبالتالي يمكننا القول ان الباعث المقترح يمكنه ان يعمل جيدا في نطاق حراري واسع يكون ما بين 600 الى 2100 درجه مئويه .

كلمات المفتاح: أنظمة التحويل الضوئي الحراري , امتصاص واسع, الباعث الانتقائي, الغير الحساس للاستقطاب

الخلايا(*GaSb/* InGaAsSb */InAsSbP)*,**HFSS**

Outline of the thesis

Chapter 1: Firstly, starting with a short historical brief of the Thermophotovoltaic (TPV) conversion system. Then, the functionality of TPV systems, their different components: Heat sources, the spectral control concepts (selective emitters, filters). Further, low-gap TPV cells are presented near close by their classification.

Chapter 2: This chapter presents an important aspect of metamaterials research. The definition of metamaterials along with historical overview is briefly discussed. The recent interest in metamaterials and progress in the development of this research area is briefly discussed, Moreover, we elucidate three major categories of electromagnetic MTM, namely electric MTM ($\varepsilon < 0$), magnetic MTM ($\mu < 0$), and negative index of refraction ($n < 0$) MTM.

Chapter 3: consecrated for numerical simulation of selective MTM design based on the finite-element method (FEM), a detailed discussion of their various characteristics such as Absorption, polarization sensibility for different incidence angle, then the overall conversion efficiency of the TPV system has been computed for a wide range of operating temperatures (600 up to 2100°C). Noteworthy, involving the MTM absorber/emitter the emittance shape can be tailored for the external quantum efficiency (EQE) of TPV cell commonly used and exhibits a low emittance in the rest of the spectrum leading to high TPV conversion efficiency.

Chapter 1: Thermophotovoltaic energy conversion

1.1 Introduction

Our aim in this chapter is to look into the fundamental model of the thermophotovoltaic (TPV) conversion system and clarifying their constitutive components, such as the potentially used heat sources, the spectral control mechanism (selective emitter, filter…), with some advantages compared to conventional solar PV. In the far-field of their development during the last years, we will be exposed and showing the current challenges facing TPV conversion systems, with the recent outlook which can in advance improve the efficiency of TPV conversion by meeting the requirements of earlier enhancement techniques, which may give feature ideas of major keys for the TPV efficiency improvement.

1.2 The importance of Thermophotovoltaic conversion

In modern industrial society, the most energy is all consumed in the sectors of transportation: industry and building, also combustions are the main sources of this energy, the use of combustions has guided to worldwide concerns about the security of supplies, increasing energy demands, limitation of resources for both (global and local) environments impacts (e.g. the critical acid rain and the climate changes) [1]. A consequence is increasing of interest in non- combustion energy-resources and the efficient use of combustions. And potentially, the TPV system can convert the heat into electricity with Carnot's perception of energy conversion, which would make it an alternative and attractive to the existing generation of electricity technologies [1].

The technique of TPV conversion has inherently some of the technological properties which can make it advantageous compared to the existing routes supply of electricity [1]. The disadvantages of central power generation are large amounts of waste heat during the conversion. Even for modern combustion-powered and combined cycle power plants discharges are about half of their inputs as waste heat. Many other disadvantages include the complexity of the system, the issues of security supplies for example the blackouts, and the distribution, transmission losses. Even so, down-scaling of central power supply technologies is essential inefficiency reduction terms, higher maintenance with high noises. Renewable generators (wind, solar PV) can replace large scale of fossil power plants. Furthermore, their widespread can requires economic high power and high scale of electrical capacity storage systems which have been not identified yet, another possibility depends on the utilization of more stabilized renewable sources for more remote locations [2].

On the small scale range of power, most likely at the order of hundreds of watts few mills of watts, on the other hand, a large amount of non-grid connected to the electricity originates from rechargeable batteries, which have some disadvantages in terms of a limited lifetime, as the slow charging process also low gravimetric energy density (MJ./kg). Hydrocarbon fuels have in the order of 100 times higher gravimetric energy densities and it can be easily stored and quickly supplied [2].

1.3 Comparison of TPV with PV technology

A TPV system uses the same principle of the photovoltaic (PV) conversion, but the main energy source in the near-infrared radiation of the emitter that can heat up by the external energy source such as combustion of nuclear fission, liquid fuel, or even gas, as it is shown in figure 1.1, the decay of a radioactive isotope or even the waste heat of furnace for glass production, etc.[3].

The real main differences for both TPV and PV systems are [4]:

- The temperature level, with high power output devices with $1W/cm^2$ of output powers, has already been fabricated and these are much higher than e.g. PV solar cells for which the output power is only $20mW/cm^2$ $kW.m^{-2}$.
- The distance source of the general electromagnetic radiation, in photovoltaic systems (PV), the sun generates an almost blackbody radiation at the temperature of like about 6000 K for a distance of 150×10^6 km, besides in TPV systems the radiators/emitters emits at a sensibly lower temperature range of (1500 to 1800 K) for distances of the order of a few centimeters, as we illustrate in figure 1.1, [5],[3].

- Supply and demand are in phase – circumvents one of the biggest problems of solar energy generation that it happens only when the sun shines. Hybrid solar thermal systems can be used, some of which have already been implemented. In such a system the excess heat from solar panels is stored using molten salts or even oil. TPVs can then be used to generate electricity when it's dark [6].

- Versatile fuel usage ‑ not only solar energy can be used to power TPV systems, but also waste industrial heat, gas burners, in principle even nuclear generators.
- TPV has a light-weight and no moving parts which means that devices are quiet and low-maintenance, which makes them perfect for use in remote locations or as portable power sources i.e. for military applications.

The main problems currently exhibited by TPV systems are the quality of the TPV converter cells themselves and not efficient enough for cooling the devices. A cooling system could be used for simultaneous heat generation, while more research needs to be done on improving the quality of the cells and spectral control components of TPV conversion.

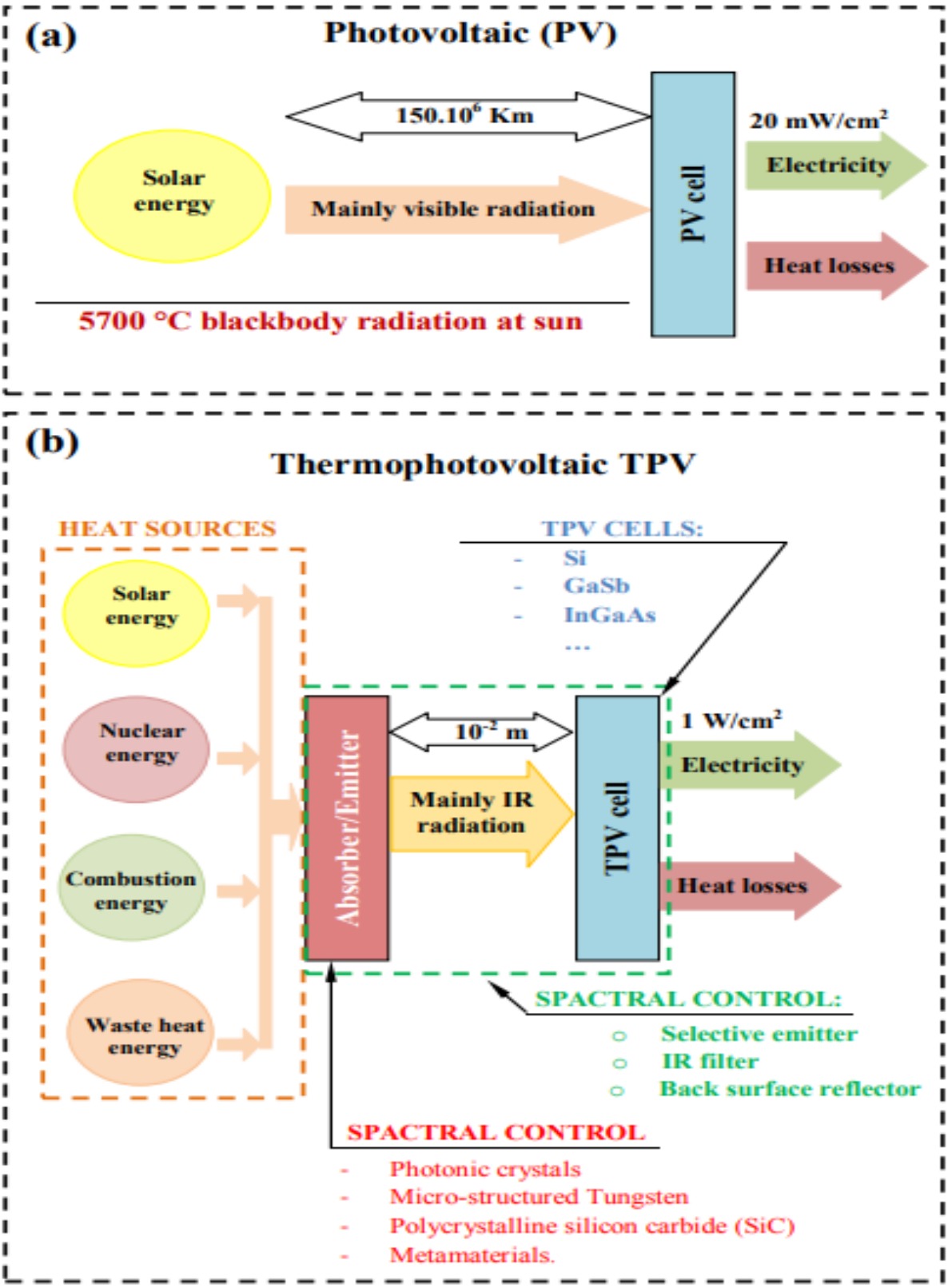

Figure 1. 1 : Photovoltaics versus thermophotovoltaics [7]

1.4 Operating principle of the TPV system

1.4.1 Components of the TPV system

TPV generation of electricity is a highly interdisciplinary technology. The conversion process of thermal radiation coming from the heat source into electricity includes several thermo-physical phenomena related to the different parts of the TPV system.

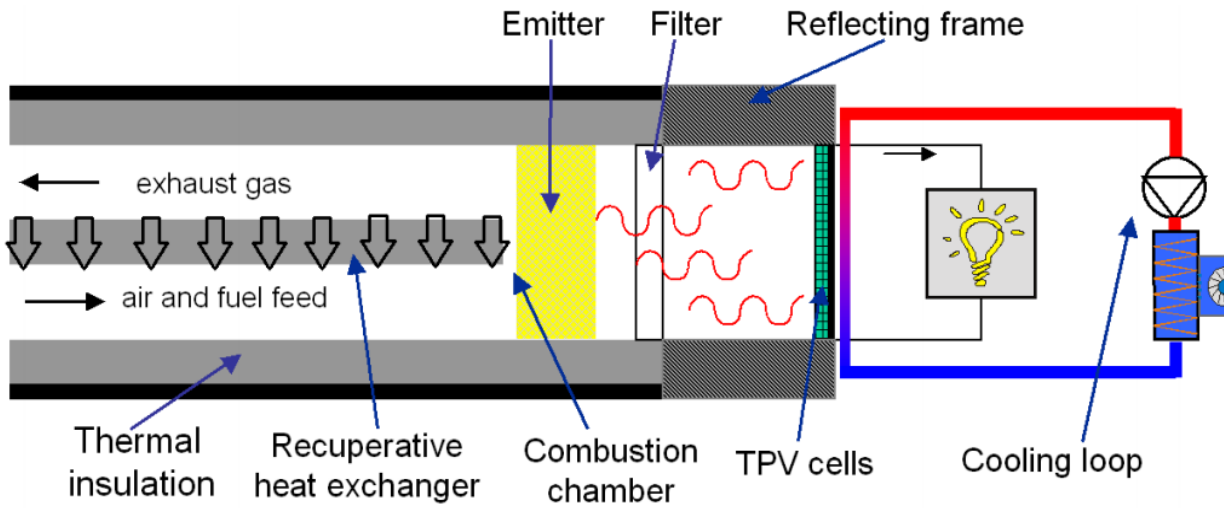

Figure 1. 2 : Simple scheme of a fueled TPV system [7]

A TPV device is composed of the main following components [4], [7]:

- **Heating system:** it releases the heat power required to heat up the emitter component. In a TPV device all the different heating techniques can be used to supply the thermal power (e.g. recuperative burner, solar concentrator, a nuclear reaction);

- **Optical system:** it is composed of an emitter, filter, and a reflecting frame used to minimize the radiation losses between emitter and cells. The main function of the optical system is to convert heat power of the heating system into radiation and transfer it to the cells, that realizing at the same moment a spectral selection of radiation.
- **Thermophotovoltaic cells:** they convert radiation to electrical power. Their design is slightly different from the normal PV cell because the radiation density is very high. For the same purpose, it's fundamental for keeping down their temperature using a cooling system to avoid their damaging.

In Figure 1.2 an example scheme of a fueled-TPV system is shown. In this case, the heating system consists of a recuperative heat exchanger and a combustion chamber. Since a TPV device is composed of different components, its total efficiency can be seen as the product of all the efficiencies related respectively to each single energy transfer that takes place in the system.

1.4.1.1 Heat sources available for TPV

A remarkable advantage of the TPV technology is the possibility to use any blackbody heat source to heat up the absorber/emitter part. The only requisite is that the temperature energy should be enough for the TPV conversion, which makes TPV a supple technology. Numerous studies for TPV structure have been proposed based on different conventional and nonconventional heat sources. We can recapitulate it in [4]:

- **Nuclear-fuelled TPV**, based on a radioisotope general-purpose heat source (GPHS), was conceived for deep space missions[8].

- **Bio-fuelled TPV**, based on the combustion of wood-powder[9].
- **Concentrated Solar TPV**, in which the solar radiation is concentrated on a TPV cell by an optical system (mirrors or lenses) and can reach a concentration ratio up to X 4600. [10].

- **Heat source realized by combustion of either gaseous fuel** (e.g. methane, propane, natural gas) or liquid fuel (i.e. diesel, hydrocarbon fuels) [11].

Thermal radiation is emitted by the bodies because of their temperature. And by definition, a blackbody is considered as a perfect absorber of radiation. It's an ideal concept since all substances will reflect some radiation. A blackbody is also considered as a perfect emitter of thermal radiation.[12]

The full power emitted by a blackbody (thermal heat sources) per unit bandwidth per unit area ($Wm^{-2}\ m^{-1}$) is given by the Planck's law of radiation [7], [13]:

$$E(T_{BB},\lambda) = \frac{2\pi.h.c^2}{\lambda^5}.\frac{1}{(e^{\frac{hc}{\lambda KT_{BB}}}-1)} \tag{1.1}$$

Where λ is the wavelength (m), T_{BB} is the blackbody temperature (°C), h represents Planck's constant (6.626×10^{-34} Js), c is the speed of the light (2.98×10^{8} m/s), and K is the Boltzmann's constant (1.380×10^{-23} JK). The total power density emitted by a thermal source corresponds to the total thermal radiation emitted over the entire wavelength spectrum.

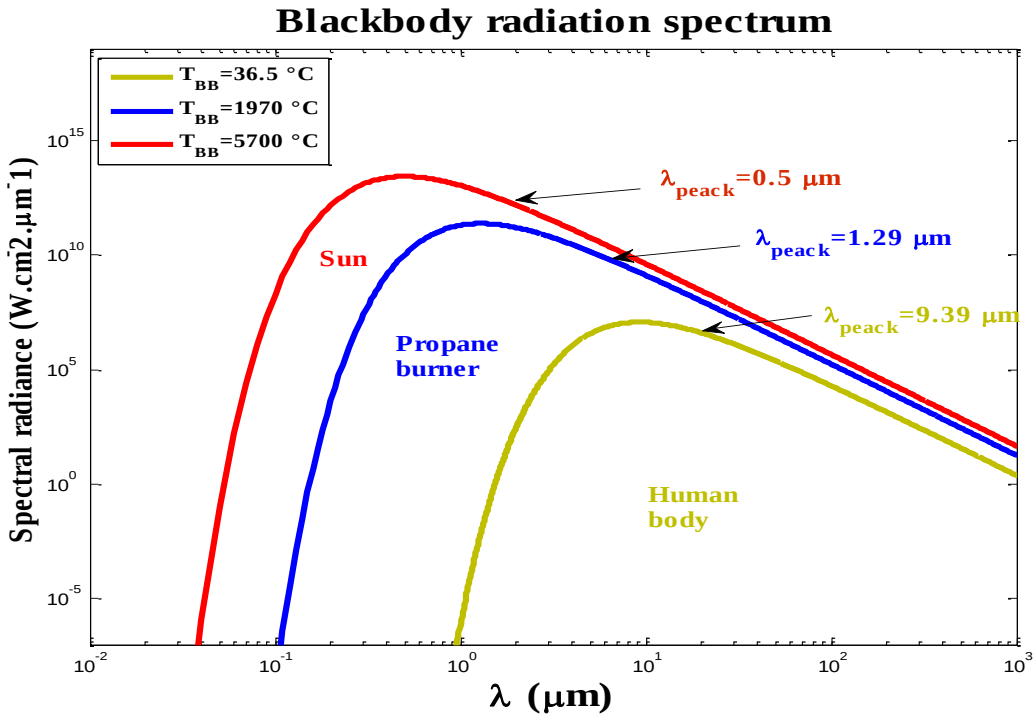

Figure 1. 3 : Spectral radiance for selected blackbody temperatures (T_{BB})[13].

Also, we illustrate in figure 1.3 the spectral emittance of a blackbody that is given by Equation (1.1), objects with selected maximal temperatures for Solar cells (red line), TPV devices (blue line), and IR photon detectors (green line). It can be observed that a considerable difference between the lowest emission wavelengths at around 5700 °C highest and the at around 36.5 °C.

1.4.1.2 Spectral control components

Spectral control is really essential for the successful energy conversion using the TPV cells. The useful radiant energy for the conversion of TPV is a fraction (most of the time is less than that) of the global radiant energy. If we take an example, only about 27% of the total radiant energy can be converted to electricity for about 950 °C TBB (blackbody temperature) and a 0.52 eV TPV cell band gap. The rest of the radiant energy 73% cannot be converted to an electricity [14], and this unconvertible energy must either suppressed from being emitted from

the source or reflected all back in order to increase TPV efficiency. And Without a spectral control, we can say TPV conversion energy performance has suffered dramatically, efficiency simplified is equal to the product of total cell efficiency and also spectral efficiency we can describe it as follows:

$$\eta_{TPV} = \eta_{cell} \times \eta_{Spectral} \tag{1.2}$$

η_{TPV}: the efficiency of thermophotovoltaic system

η_{cell}: the efficiency of TPV Cell

$\eta_{Spectral}$: the efficiency of spectral control

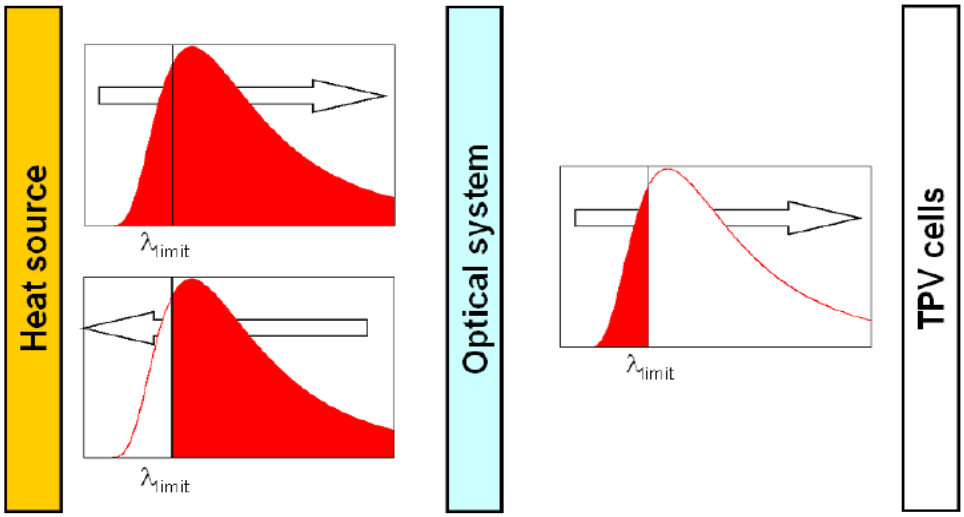

Figure 1. 4: Operating principle of TPV spectral control [7].

An elementary design representing the optical system concept is shown in figure 1.4 describes how exactly the optical system can improve efficiency. A spectral control mechanism can be explicated as a system that emits only the wavelengths correspondence of $\lambda < \lambda gap$ and reflects back all wavelengths have $\lambda > \lambda gap$. That would mean higher conversion efficiency.

(I.e. The net efficiency conversion for a 30% efficient TPV cell without the spectral control would be less than 8 % (30% x 26% = 8 %) for like 950°C of Blackbody temperature. On the other side, if we have an 80 % efficiency of spectral control, the net conversion efficiency would be about 24 % (30% x 80% = 24%) for the same exactly TPV cell[14].

1) Absorber/Emitter

This component is also called (radiator) and can be either broadband or selective absorber/emitter. It may be classified according to different aspects including the following[1]:

- Optical properties (e.g. absorption, emissivity, polarization sensitivity).
- Thermal properties (e.g. melting point, upper operation temperature, evaporation rate).
- Electrical properties
- Material composition.
- Design shape (e.g.1D, 2D, and 3D Photonic crystals (PhCs) structure. micro-structured).
- Availability and economics

In a conventional TPV system: oil, gas or even wood burners can be used to heat up the absorber/emitter. These burners are commercially available for large scale power range from a several kW to few MW for immobile applications [15], essentially the newest absorber/emitter technology for TPV application can be summarized in four different innovative prototypes:

- Silicon Carbide (SiC) one of the most used materials as broadband ceramic absorber/emitter, which has a good emittance, around 0.9%, over the whole infrared spectrum [16].

- An advanced approach to design selective absorber/emitter is the use of, 1D, 2D, and 3D Photonic crystals (PhCs) structure. PhCs intervene by his optical band-gap to suppress the (emissivity=emittance) in a specific spectral range depending on the periodicity of the unit cell structure. Experimental results are given by Celanovicet al, the increase of the selectivity of tungsten surfaces involving PhCs band-gap proprieties [17].
- Micro-structured tungsten is another way to produce a selective emission for TPV applications; this absorber/emitter is recommended for operation in a TPV system with GaSb. Unfortunately, the design holds a complex conception method and a strong angle dependence of the emittance [18].
- Recently, numerous theoretical and experimental studies have been performed on high-temperature selective emitters that can help reach the 24% efficiency. Various methods, including selective metamaterial emitter (SME), selective meta-surfaces (FSSs) , etc. [19].

2) Optical Filter

Optical filters mostly are placed in the middle of the emitter and the photovoltaic cell, as well as reflectors deposited on the backside of the photovoltaic cell, which reflect all the wavelengths mismatched with the cell's band-gap. Filters for TPV can be divided into four different categories [7]:

1. Quartz glass: it acts as an absorptive filter, having high emittance values in some wavelength and high transmittance values in the rest. Usually, a Quartz glass is used in

a TPV system to protect the TPV cells from the high temperature and realize a first selection of the radiation reducing the thermal charge on the cells[13].

2. Interference (or dielectric) filters: low-pass filters realized as a multilayer stack of thin dielectrics film, basically it's created by two materials, one with high and the other with low refractive index [1].
3. Plasma filters based on Transparent Conducting Oxides (TCOs): called Plasma filters consist of a highly doped semiconductor layer, they have optical properties with a reflectance range like metals and low absorption range like insulators[8].
4. Frequency Selective Surface (FSS) filters: also called meta-surfaces filters (MSs), realized as an array of metallic nano-scale patch deposited on a dielectric substrate. They have spectral selection properties that make them excellent candidates for TPV applications[20].

1.5 TPV cells technologies

The main use of TPV cells is based on the photo-generation of electrons and separation of charge carriers. When a photon hits a semi-conductor material with energy greater than the semiconductor band gap it can generate an electron-hole pair: the photon energy is absorbed by an electron with the highest energy level and bounded to neighboring atoms (electron in the valence band) exciting it to an energy level where the electron is free to move and generate current (conduction band). The hole generated by the absence of an electron can be occupied by another electron in the valence band [13]. The average distance traveled for the charge carriers before recombination is called diffusion length. The bandgap of a semiconductor material (i.e. the cell bandgap E_g) corresponds to the energy gap between the valence band and conduction band energy levels; as is seen in Figure 1.5.

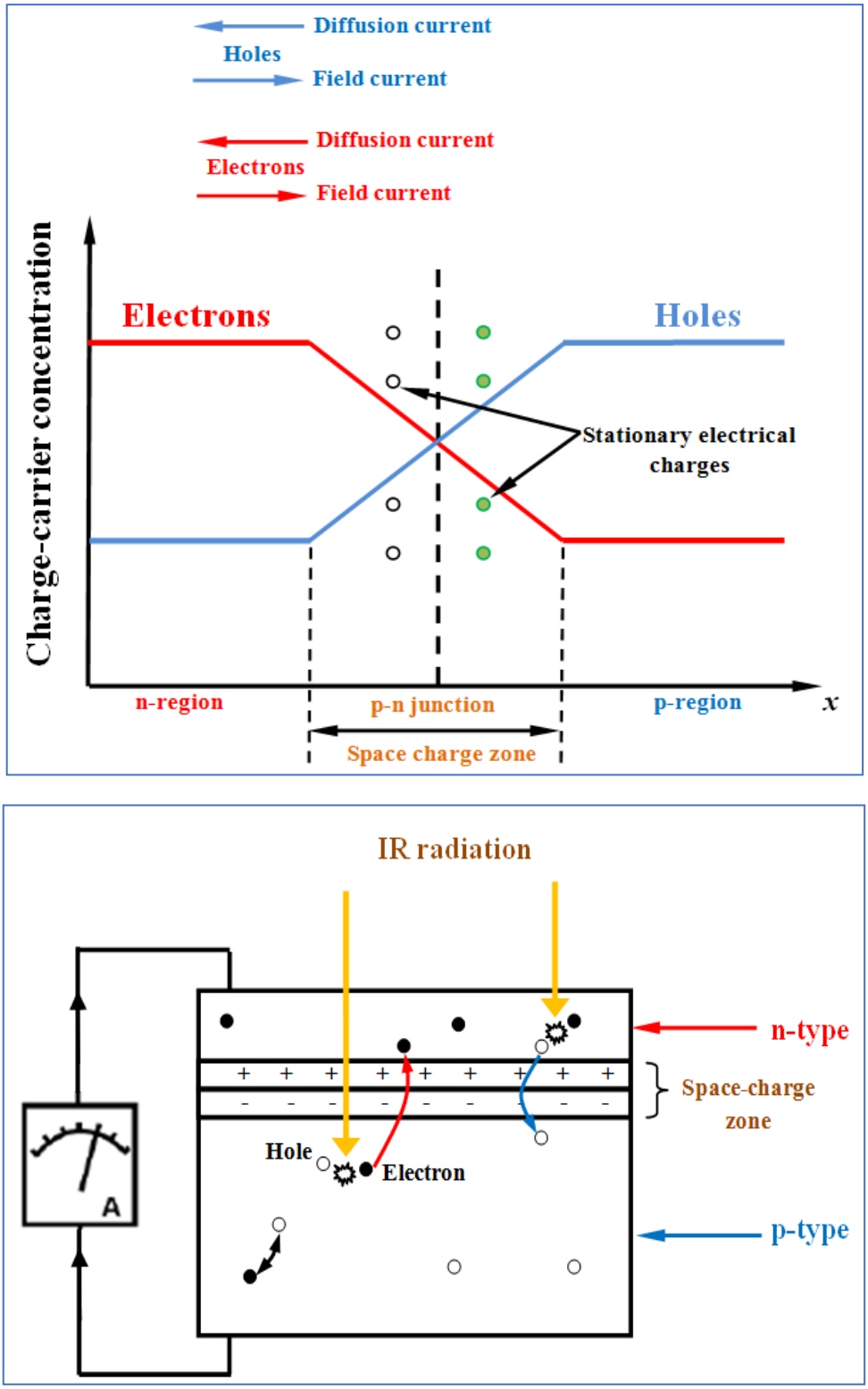

Figure 1. 5: Distribution of charge carriers at a p-n junction and operating principle of a TPV cell [7].

The photo-generated charge carriers are separated by the p-n junction sector in the cell, which consists of a layer of the n-type (high number of electrons) and a layer of the p-type (high number of holes) put together in close contact. TPV cells are large-area p n junctions.

The electron in the n-type layer generates diffusion of electrons in the p-type layer and recombination with the holes present in it. This diffusion current is balanced by an electric field caused by the unbalanced charge distribution. In the same conditions, the area close to the junction called (space-charge zone) does not have any moving charge carrier. The electric field produced by diffusion acts as a separation zone in case that an electron-hole pair is produced after absorption of a photon with energy large enough: if the pair is generated on the p-side the electric field accelerates the electron into the n-side and vice versa if the absorption takes place in the n-side the generated hole is brought into the p-side, as shown in figure 1.5.

In the TPV cell, the photo-generated current is maximal when there is no connected load. When connecting the load to the TPV cell, the photo-generated current due to cell illumination results in negative voltage, and the current-voltage characteristic I(V) curve of a diode is described by Shockley diode equation [13] :

$$I_{diode} = I_0\left[\exp\left(\frac{qV}{KT}\right)-1\right] \tag{1.3}$$

q: electron charge (1.6×10^{-19} C).

V: the voltage across the diode.

k: the Boltzmann ‘s constant.

T represents the absolute temperature(K).

I_0 represents diode current saturation.

1.5.1 Characteristics parameters of TPV cells

The main characteristics of TPV cell are: open circuit voltage (V_{oc}), short circuit current (I_{sc}) and maximum power point (V_{mp}, I_{mp}). The maximum power that achieved from TPV cell is occurs at a point on the bend in the I-V curve known as the maximum power points [7].

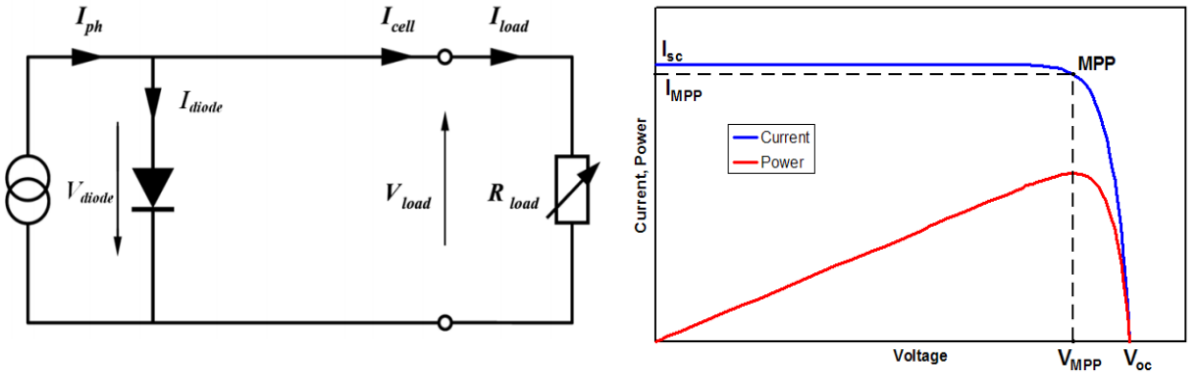

Figure 1. 6 : Equivalent circuit of an ideal TPV cell, and qualitative (IV) and power curve of a TPV cell [13].(correct the schema

The equivalent circuit for an ideal TPV cell, therefore, consists of a photocurrent source I_{ph}, a diode, and a resistor R_{load} connected in parallel as shown in Figure 1.6. The current flowing through the load in the ideal case results [21]:

$$I_{cell} = I_{ph} - I_{diode} = I_{ph} - I_0 \left[\exp\left(\frac{qV}{kT}\right) - 1\right] \quad (1.4)$$

The power increases by the increasing of the load, getting a maximum at the so-called maximum Power Point (MPP) in correspondence of the maximum current (I_{MPP}) and voltage (V_{MPP}), at the point called open circuit voltage (v_{oc}). Under a constant blackbody radiation, and for higher values of E_g, I_{sc} decreases, and we receive less photons with energy higher than

E_g, whereas V_{oc} increases. One more essential parameter of the photovoltaic characteristics is known as the Fill-Factor (FF). The fill factor determines the quality of the TPV cell. It operates way better when the FF value is close by to unity [10].

$$FF = \frac{V_{MMP} \times I_{Mpp}}{V_{OC} \times I_{SC}} \tag{1.5}$$

Figure 1.7 shows the equivalent circuit of a real TPV cell, with a series resistance (Rs) representing the material resistance and the resistance cell surface metallic contacts, and a parallel resistance (R_p) representing leakage currents due to impurities causing by a partial shorting of the p-n junction, is described by Equation (1.6) [21].

$$I_{cell} = I_{ph} - I_0\left[\exp\left(\frac{q}{KT}\left(V_{load} + R_s.I_{cell}\right)\right) - 1\right] - \frac{\left(V_{load} + R_s.I_{cell}\right)}{R_p} \tag{1.6}$$

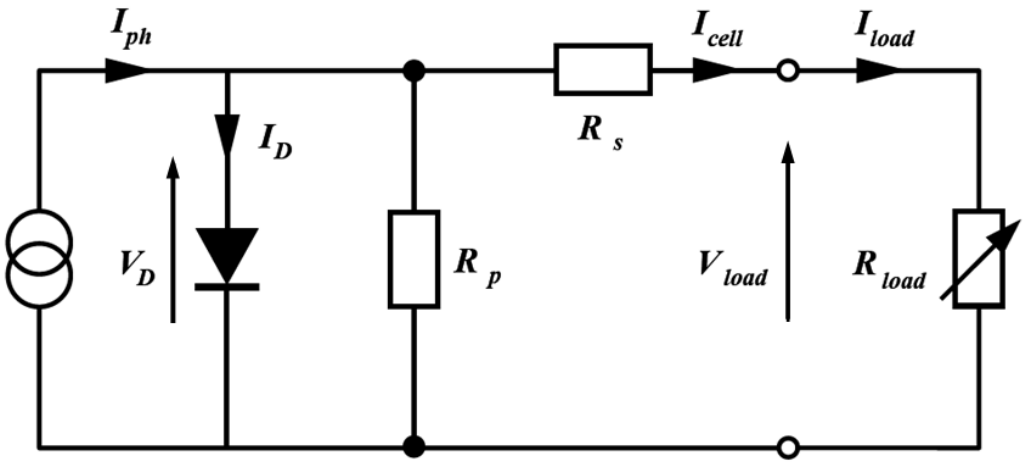

Figure 1. 7: Equivalent circuit of a real TPV cell [13].

An additional important factor that influences the performance of the cell is the cell temperature, generally taken into account by using cell temperature coefficients, which are experimentally measured and calibrated the percentage variation of the cell parameters compared to temperature level [22].

The open-circuit voltage is calculated as follows:

$$V_{oc} = \frac{nkT_{cell}}{q} \times \ln\left(\frac{I_{SC}}{I_0} + 1\right) \tag{1.7}$$

Where n is the ideal factor, T_{cell} is the cell temperature and I_0 is the reverse saturation current.

The V_{mp} of the fill factor in the equation (1.5) is calculated as follows:

$$V_{MP} = V_{OC} - \frac{kT}{q} \ln\left[\frac{V_{MP}}{\frac{kT}{q}} + 1\right] \tag{1.8}$$

Finally, the TPV conversion efficiency can be calculated as follows:

$$\eta = \frac{I_{SC} \times V_{oc} \times FF}{P_{inc} - P_{ret}} \tag{1.9}$$

where P_{inc} expresses the power of radiation from the TPV cell, P_{ret} is the power reflected by the cell. The energy efficiency of the system is calculated as follows [23]:

$$\eta_e = \frac{P_{cell}}{P_{Inc}} \tag{1.10}$$

η_e : refers to the system efficiency, the power generated by the P_{cell} TPV system. Calculation of the short circuit current density J_{sc} (A/cm²) of the cell under a well-defined blackbody spectrum. Can be expressed as [23]:

$$J_{sc} = \frac{1}{hc}\int_0^{\infty} e(\omega) EQE(\omega) d\omega \tag{1.11}$$

Where e (ω) is the emittance of the emitter, with h being the Planck‘s constant and c the light speed, the measured external quantum efficiency (EQE). That describes how efficiently the incoming radiation is converted into electricity. Specifically, it is the ratio of carriers collected from the solar cell to the number of incident photons of a certain energy. An example of a quantum efficiency plot is shown in figure 1.8.

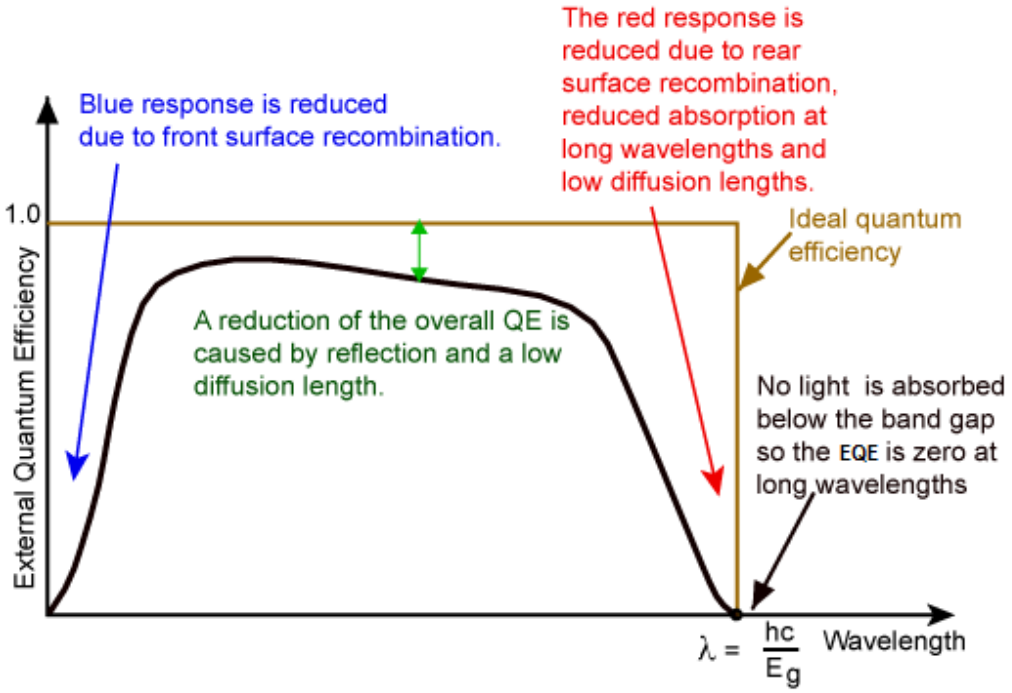

Figure 1. 8 : An example of external quantum efficiency plot solar TPV cell vs. ideal quantum efficiency as a function of the wavelength of incoming photons [11].

In an ideal case, if all the photons at a specific wavelength are absorbed and resulting carriers are extracted, the EQE is equal to 1. No light is absorbed below the bandgap so the EQE is zero for longer wavelengths. For real cells, EQE is reduced due to recombination effects. The annotations in figure 1.8 explain in detail which processes are responsible for reducing the EQE at specific wavelengths. External quantum efficiency (EQE) is often measured for practical devices. It includes optical losses such as reflection of the front surface. It allows for

a realistic estimation of the performance of fabricated cells after all loss mechanisms have been included. By measuring the reflectance and transmission of the devices, the internal quantum efficiency (IQE.) can be calculated from the EQE results.

1.5.2 TPV cell classification

As well, we can classify TPV cells in high, middle, and low-bandgap cells:

- High-band gap TPV cells: for the reason of their high-band gap, these cells have limited efficiency and require a very high blackbody temperature (over 1500°C) to reach acceptable power density outputs [19].

- Middle-band gap TPV cells: This kind of TPV cell corresponds to the spectrum peak wavelength in the case of a blackbody at 1300°C. Cells with Eg ~0.7 eV is the most investigated for middle TPV systems; diverse hetero-structures are developed with an E_g ranging from 0.53 to 0.73 eV [24].

- Low-band gap cells: Cells with ($Eg \leq 0.53$ eV) has been investigated and developed recently and seems attractive for low-temperature applications (less than 900°C), this category suffers from low V_{oc} voltage with poor fill factor FF [25].

Year	Material	E_g(eV)	J_{sc} (A/cm^2)	V_{oc} (V)	FF(%)	T_{BB}(°C)	References
1997	InGaSb	**0.7**	0.8	0.38	66	1100	[26]
2000	InGaAsSb	**0.53**	3	0.344	-	1400	[27]
2003	GaSb	**0.72**	3	~0.41	-	Below 1400	[28]
2003	InAsSbP	**0.45**	3	0.15	-	1000	[19]
2003	InGaSb	**0.56**	3	0.26	-	1200	[29]
2004	Two-junction (InGaAs) Junction 1 Junction 2 Total	 **0.74** **0.63** 	 0.303 0.461 0.296	 0.448 0.284 0.724	 61 52 73	 954 	[30]
2004	Ge	**0.66**	10	0.43	-	1500 to 1900	[24]
2006	$InGa_{0.53}As_{0.47}$	**0.74**	1	0.465	64	1000 to 1800	[31]
2006	InGaAsSb	**0.53**	2.9	0.306	67	1800	[25]
2009	$InGa_{0.69}As_{0.31}$	**0.6**	2.26	0.355	66.5	1800	[32]
2011	$Ga_{0.03}In_{0.97}As_{0.81}Sb_{0.13}$	**0.34**	0.29	0.028	33	1000 to 1500	[33]
2013	InGaAs	**0.74**	0.288	0.405	65	Below 2900	[34]
2016	InAs	**0.32**	1.32	0.38	37	Below 1000	[35]
2016	GaSb and GaInAsSb	**0.5 ~ 0.53**	6	0.55	80	800 - 1800	[34]

2017	GaSb/GaInAsSb	**0.53**	7.87	0.8	82	1000 - 1800	[36]
2019	GaAs/GaInAsSb	**0.53**	1.04	0.214	53	800	[37]

1.6 Advantages and limits of TPV system

After describing and presenting the different processes and components that they are involved typically in a TPV system it makes sense to recall briefly the primary characteristics of TPV is pointing out why TPV can be an attractive and interesting energy conversion technology. The potential advantages of this technology are the followings [13]:

- Robust and reliable technology: in TPV system there are no moving parts, therefore low maintenance is required.
- An important power density output: power densities higher than 1 Wcm^{-2} can be obtained, a hundred times or even more high than normal PV.
- Any heat source can supposedly be used to heat up the absorber/emitter.
- High cell efficiency thanks to the spectral control system (i.e. Absorber/Emitter, filter…).

Also, we display in figure 1.9 the principal phenomena that limit the TPV efficiency. Not all the incident photon energy is useful to generate an electron-hole pair, but only that part necessary to overcome the E_g of the TPV cell. The excess photon energy is dissipated as heat into the semiconductor.

Table 1. 1: Development of TPV cells technologies [7].

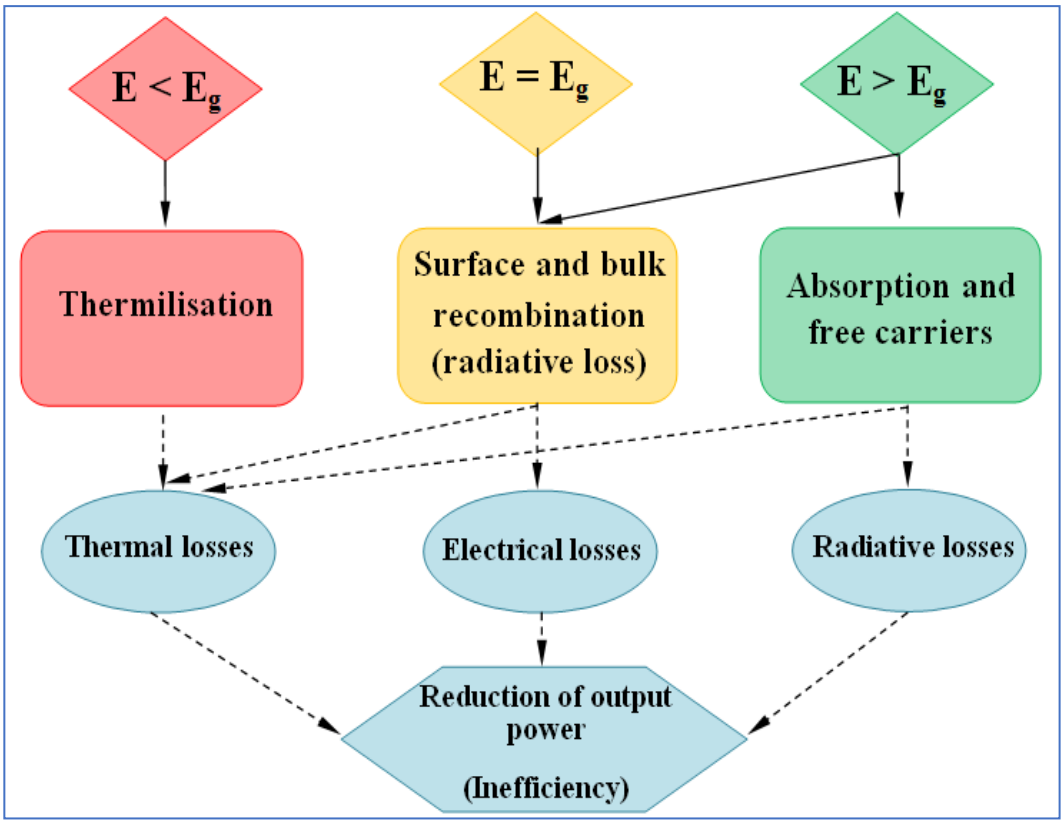

Figure 1. 9 : The principal phenomena losses in the TPV conversion system[38]

There are two main types of loss mechanisms in TPV cells in this case; optical losses and electrical losses. Main optical losses include reflection off the front surface of the cell, shadowing by the top contacts, sub-bandgap losses, and lattice thermalization by the very high and very low energy photons. Reflection losses can be minimized by texturing the surface of the cell to accept photons coming from a large variety of incident angles and randomize the angle at which they enter the cell. Together with a back surface reflector, surface texturing (e,g Metasurfaces) can be used to significantly extend the optical path of photons inside the semiconductor and hence further improve the absorption probability. This technique is called light trapping. Sub-bandgap (thermalization) losses originate from the fact that photons with low energy will not be absorbed in the cell, therefore not all of the incident spectrum can be used which results in a reduction of the output current. It is hard to

circumvent this issue with single-junction cells, however multiple cells with different bandgaps connected in parallel can be used to maximize the absorption spectrum (multi-junction cells), or by introducing an intermediate emitter (selective emitter). Electrons with high energies cause the last of the optical losses, lattice thermalization. Energy equal to the bandgap of the material is used to excite an electron to the conduction band while the excess energy is dissipated as heat. This causes an increase in the temperature of the cell causing the generation of more defects, lowering the bandgap, and hence reducing the output voltage.

The most important electrical loss for TPV is Auger recombination since it is most significant in low bandgap materials with higher carrier densities, where the interactions between carriers are stronger. In Auger recombination two similar carriers collide, one of which is excited to higher kinetic energy and the other recombine across the bandgap giving its energy to another carrier. Eventually, the excess energy is lost as heat contributing to the thermalization of the lattice. The Auger recombination is unavoidable since it is intrinsic to the physical processes within the material.

Another type is Shockley-Read-Hall (SRH) recombination involving trap states in the bandgap. Trap states “capture” free carriers slowing down the carrier transport through the material. They can be released through thermal activation or annihilated if an opposite charge is captured before the first one is released. In the second case, the traps are called recombination centers. Trap states arise from defects in the crystal lattice of the semiconductor. These can be caused for example by thermal cracking, surface states, or lattice mismatch between subsequent layers resulting in stress build-up and hence the formation of dislocations.

1.7 Conclusion

In this chapter, a short review of how TPV system works with a brief historical showing how important it can by in different aspects, The advantage of those systems compared to conventional solar PV systems is that it is possible to control the emission properties of the radiator to increase the performances of the system can lead to acknowledging some of the features proprieties and ideas, We spelled out the essential TPV components, and their diversity such as: the used heat sources (blackbodies) in; the spectral control devices, absorber/emitters, and filters then we describe how semiconductor TPV cells can be improved playing on bandgap and all electronic parameters. As the last point, the TPVs technologies remain a very attractive renewable field, which should be investigated further. Due to new developments as well as to a growing application field for TPV devices wide-spread commercialization might occur soon.

Chapter 2: Overview of Electromagnetic Metamaterials.

2.1. Introduction:

This chapter introduces the concepts of electromagnetic metamaterials (MMs) with a short historical review, furthermore, they have an exceptional electromagnetic and optical property and not mostly exist in nature such as negative permittivity with a ray of wires (and/or) permeability with split-ring resonators (SRR), and negative refractive index. Therefore, we studied the basic theoretical aspects of electromagnetic wave propagation in matters, and their interaction in different materials such as tungsten (W) which are essential to know the term plasmonics or Plasmonic metamaterials alongside with dielectrics which were required in our studies especially in selective emitter/absorber. The design methodology has been proposed using the HFSS 3-D solver, and MATLAB.

2.2. History of Metamaterials

Although the word metamaterials (MMs) was first introduced by Smith in 2000 [39], their earliest application can be traced back to the fourth century AD, when people first used MMs to decorate pieces of art; for example, the Lycurgus Cup made using ruby glass with gold nanoparticles embedded. In 1898, Bose manufactured a kind of "twisted jute" material consisting of period sub-wavelength meta-atoms with an artificial chiral effect. This is the first significant MMs structure engineered by modern technology [40]. In the 1940s – 1960s, scientists focused on the interaction between microwave radiation and artificial dielectrics with periodical arrays of metallic plates wires, and spheres [41], [42]. In 1968, a milestone paper in electromagnetic MMs research was published by Veselago [43]. In his paper, Veselago pointed out that the electric field vector (E), magnetic field vector (H), and the wave vector (k) formed a left-handed system. Therefore, a MMs was essentially a left-hand material (LHM) that did not obey the right-handed law, like normal materials [43].

Veselago's prediction was first proved by Smith in 2000 [39]. Also in 2000, Pendry demonstrated that it was possible to use the unique properties of MMs to manufacture the so-called "perfect lens", which was the beginning of the focus on the engineering applications of metamaterials [44]. Pendry's work filled the gap between the various novel theories of MMs and their useful application. Across the split-ring resonators (SRRS) they are artificially produced structures related to MTMs. And their purposes are to produce the required magnetic susceptibility which is a magnetic response in various types of MTMs up to 200 terahertz or even higher. These media can create a necessary strong magnetic coupling for an applied electromagnetic field (EMF), not otherwise available in such conventional materials. As an example, the effect like a negative permeability is made by coupling the periodic array and split-ring resonators [45].

Negative permittivity (ε) happens exactly when the incident wave is below or near the plasma frequency (ω_p) and strikes a metal surface. In such a case, the independent electrons can move up in a way that cancels incident waves, and the wave will be mostly reflected from the metal (more like a mirror). If the frequency of an incident wave is higher than the plasma frequency, permittivity will be positive and the electrons can't move in a way that can cancel the incident wave, so the wave will penetrate the metal [45]. Negative permittivity explains that we have enough free electrons that they can oscillate in the opposite side phase with the incident light and therefore it cancels out. As a result, the light cannot penetrate the materials with a negative epsilon so it will be reflected.

2.3. Electromagnetic classification of Metamaterials

The classification of electromagnetic MMs can be illustrated in Figure 2.1 [46];

a) Mediums with ($\varepsilon > 0$, $\mu > 0$) are called as double positive (DPS) materials or right-handed MTMs (RHM), like the most dielectrics drop under this designation.
b) Mediums with ($\varepsilon < 0$, $\mu > 0$) are called as epsilon-negative (ENG) mediums or electrical MTMs. In certain frequency regimes, like many electrical plasmas exhibit these characteristics, such as noble metals at optical wavelengths, and doped semiconductors at certain frequencies below the plasma frequency, and ferroelectric materials.
c) Mediums with ($\varepsilon > 0$, $\mu < 0$) are called as Mu-negative (MNG) mediums or magnetic MTMs. In certain frequency regimes, some gyro-tropic or ferrite materials show this characteristic.
d) Mediums with ($\varepsilon < 0$, $\mu < 0$) are called as double-negative (DNG) mediums or left-handed MTMs (LHM). This class of mediums has only been established with artificial structures. In nature, there is no such material.

e) When ε≈ 0 or μ≈ 0, MMs with near-zero refractive index or zero refractive index (NZI) can be established. The light inside such mediums do no spatial phase change and highly large phase velocity, as well as properties that can be applied for realizing selective emission, tunneling waveguides [47].

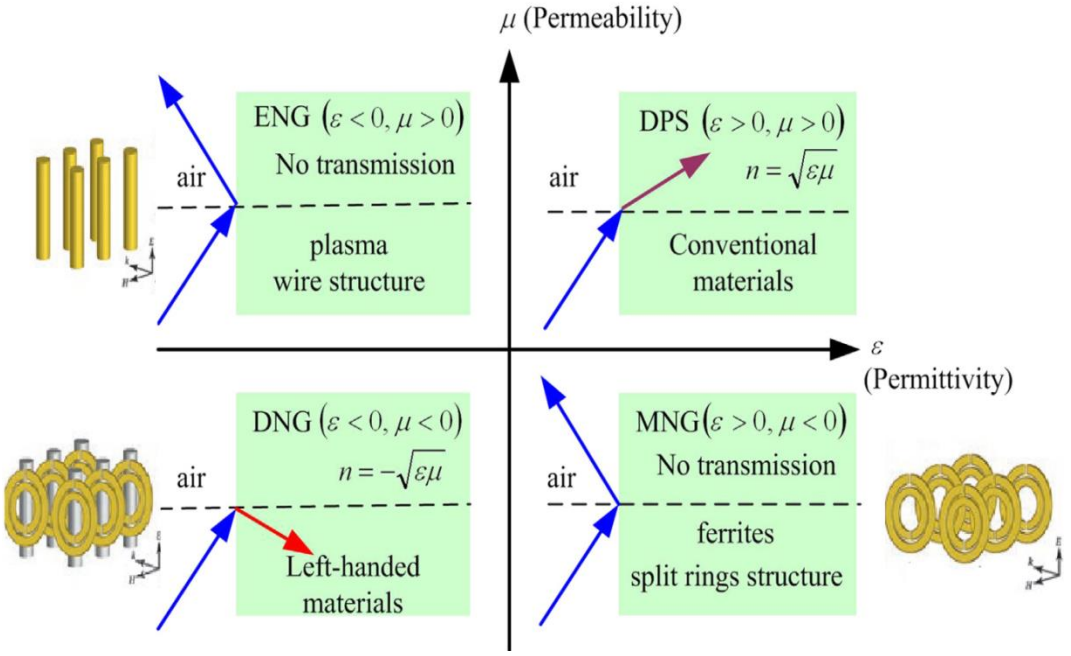

Figure 2. 1: Classification of electromagnetic MMs based on permeability (μ) and permittivity (ε).

In MMs, the material permittivity (ε) and permeability (μ) can both be negative, which induces the negative refraction index. The refraction index *n* is calculated from the following formula [48]:

$$n = \pm\sqrt{\varepsilon_r \mu_r} \tag{2.1}$$

Therefore, the refraction index *n* is also negative. This is the most important and unique property possessed by MMs, and is the foundation of the perfect lens and invisible cloak applications, which are both MMs. More interesting properties can be obtained by an in-depth analysis of Maxwell's Equations in MMs [48]. Another perspective of MMs classification is the dimensionality of the structures which form a bulked 3D design with a large number of

constitutive elements in every direction (x, y, and z). Surface (2D) materials, when the structure is a thin film with only 1 to 3 constitutive elements across its thickness. (2D) MMs are usually called meta-surface (MS) or thin films MMs. Linear (1D) structures design with nanoscale, they are also called meta-waveguides component[46].

2.4. Electromagnetic properties of constitutive materials

In a similar way of any designed electromagnetic structure, to understand the apparent extrinsic properties, we must first understand the essential properties of the constituent components of this system. In the case of infrared and optical MMs, we will combine different conventional material such as dielectrics and metals [46]. For drawing the design considered, where the dielectric acts usually the host medium that supports either structured or unstructured metallic arrays of resonators. In the case of bulk MM structures, where the resonant chips are distributed throughout the volume of the structure, and necessarily the dielectric layer needs in somewhat to be transparent. Any significant amount of dissipation would result in higher MMs losses and decreased system performance [49].

2.4.1. Properties of Metals

Recently, MMs applications have shifted from the radio-frequency (RF) and microwave to THz frequencies, the propriety of the materials used to design these structures has also changed. MTM structures such as frequency selective surfaces (FSS) that operate at RF and microwave frequencies are oftentimes constructed using printed metal (i.e. copper…) wires on top of printed circuit board material. At these frequencies, the metal is treated as a perfect electrical conductor (PEC). The materials can be thought of as having high electrical conductivity and are negligible losses, and the dielectric properties of the metal are assumed to be negligible. The electromagnetic response of metal is widely performed by the group

movement of free electrons within the crystalline structure of the metal. In this case, the electrons are considered to be freely capable to move about in the metal, without any restoring force or spring constant. Therefore, the resonance frequency from the standard Lorentz model is zero in this case, and it does not appear in this study. This model for electron motion in metal is known as the Drude free electron model. By note harmonic incident electric field (E_0. $e^{-i\omega t}$), the equation of motion for free electrons in a metal is given by [49]:

$$\vec{r}(t) = \frac{e}{m}\frac{e\vec{E}_0 e^{-i\omega t}}{(\omega^2 + i\Gamma\omega)} \tag{2.2}$$

Where *e* and *m* represent the charge and the effective mass of the electron, respectively, and Γ is the damping constant. With solving this, we obtain the displacement r of the electron from its original position:

$$\varepsilon(\omega) = 1 - \frac{\omega_p^2}{\omega^2 + i.\Gamma\omega} = 1 - \frac{\omega_p^2}{\omega^2 + i.\Gamma^2} + i\frac{\omega_p^2.\Gamma}{\omega.(\omega^2 + \Gamma^2)} \tag{2.3}$$

where ω_p is the volume plasma frequency at which the density of the electron gas oscillates [50]:

$$\omega_p = \sqrt{\frac{ne^2}{\varepsilon_0 m}} \tag{2.4}$$

The Drude model intended for the dielectric function of the metallic materials by equation (2.4) is an elegant and concise treatment especially for THz properties of metals. However, it has to be modified to adequately reflect reality. One common observation that is not predicted by the Drude model is that gold and silver, with almost identical plasma frequencies, appear so different when exposed to visible light regime [50]. some of e.g. is shown in table 2.1.

Metal	$\omega_p(eV)$	$\omega_p(10^{15}s^{-1})$	$\Gamma(eV)$	$\Gamma(10^{15}s^{-1})$
Silver	**9.2**	**14.0**	**0.0021**	**0.032**
Gold	**3.1**	**13.8**	**0.072**	**0.11**
Copper	**8.8**	**13.4**	**0.092**	**0.14**
Aluminum	**15.1**	**22.9**	**0.605**	**0.92**

Table 2. 1 The plasma frequency ωp, damping constant Γ of selected noble metals [51].

2.4.2. Properties of dielectrics

MMs absorbers consisting of metal, metal-dielectric, or dielectric materials have been realized across much of the electromagnetic spectrum and have demonstrated novel properties and applications. However, most absorbers utilize metals and thus are limited in applicability due to their low melting point, high Ohmic loss, and high thermal conductivity. To break these limitations, all-dielectric metasurface absorbers based on hybrid dielectric waveguide resonances were designed.

The fundamental physical background of wave interacting with a dielectric can be examined using the following Maxwell‘s equations [48], [7]:

$$D = \varepsilon_0 E + P = \varepsilon_0(1+\chi_e)E = \varepsilon_0\varepsilon_r E \tag{2.5}$$

$$B = \mu_0 H + M = \mu_0(1+\chi_m)H = \mu_0\mu_r H \tag{2.6}$$

Where D is electric displacement (C/m^2), B is magnetic displacement (T or Vs/m^2), E electric field (V/m) and H is the magnetic field (A/m).In a homogeneous isotropic medium, electric and magnetic displacements are given by equations[52]:

$$\overrightarrow{D} = \varepsilon \overrightarrow{E} \tag{2.7}$$

$$\overrightarrow{B} = \mu \overrightarrow{H} \tag{2.8}$$

The relationship given by two equations (2.5) and (2.6) presents the pair electric and magnetic displacement ($\overrightarrow{D}$, H) with the pair electric and magnetic field (E, B), through a couple electric and magnetic susceptibilities (χ_e, χ_m), with ε_0, μ_0 represent the vacuum permittivity and permeability, respectively, through a couple of polarizabilities electric and magnetic (P, M). We shall omit the subscript r in the relative permittivity and permeability. The interaction between electromagnetic waves and any material, essentially, involves determining the solutions of Maxwell‘s equations by using the appropriate boundary conditions.

Therefore, the equations (2.7) and (2.8) at the frequency-domain can be written as [50]:

$$D(\omega) = \varepsilon_0 \varepsilon_r(\omega) E(\omega) = \varepsilon_0 \left[1 + \chi_e(\omega)\right] E(\omega) \tag{2.9}$$

$$B(\omega) = \mu_0 \mu_r(\omega) H(\omega) = \mu_0 \left[1 + \chi_m(\omega)\right] H(\omega) \tag{2.10}$$

The majority of MMs with metal-dielectric composite are strongly dispersive [53]. In the infrared or visible wavelength regime, the origin of the dispersion in MMs is mostly ascribed to the metallic part, because metals are much more dispersive than dielectric matters. When designing a THz-MMs structure, it is important to make sure that the selected dielectric constituent is transparent within the wavelength range of interest. Moreover, it is very helpful to include the frequency influence of the dielectric function ε (ω) in metallic media.

2.5. Metamaterials contribution to nanostructures devices

The extended science of MMs to the quantum level (nanostructure MMs) has comprised quantum coherent unit elements with desired (engineered) parameters, also quantum states of

at least some of these elements can be directly controlled and it can preserve a global coherence for the duration of time, exceeding the traversal time of the relevant electromagnetic signal. These properties control macroscopic quantum coherence that makes a quantum MMs a qualitatively different system, with several unusual properties and applications [54]. Furthermore, metasurfaces are an important class of MMs Nano-structures and can be regarded as the two-dimensional equivalent of MMs, and they have many different applications depending on their constitutive materials and geometry.

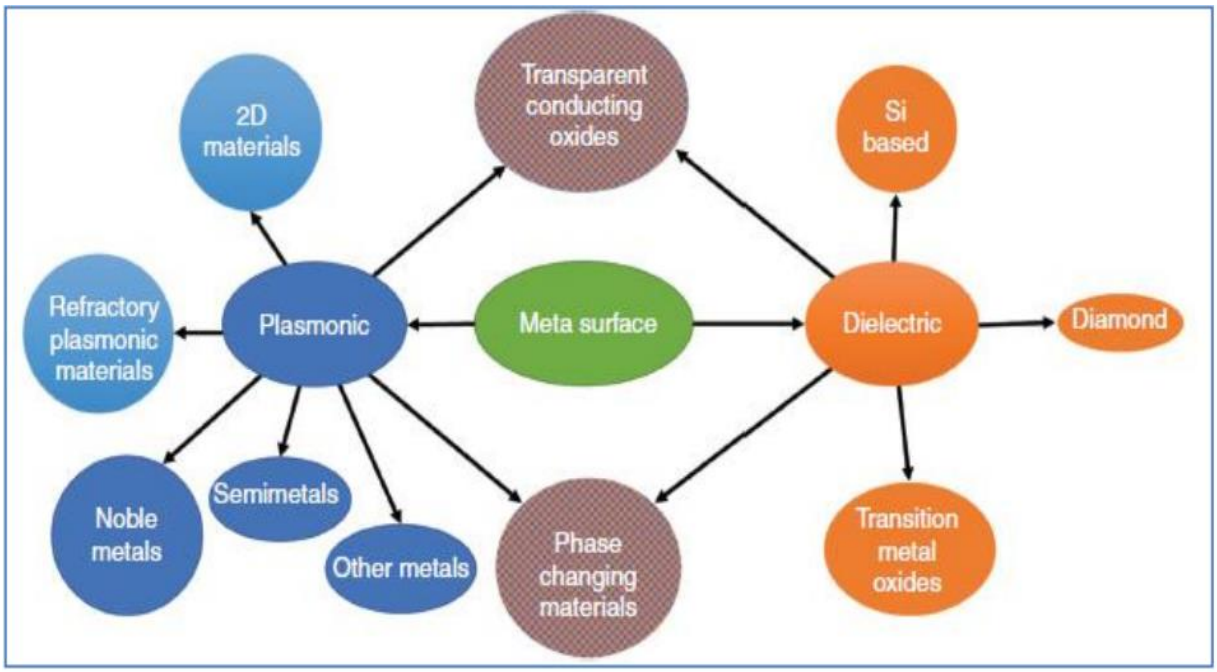

Figure 2. 2: Emerging material platforms for optical Metasurfaces including noble and other commonly used in plasmonics metals; semimetals and intermetallic compounds exhibiting metallic behavior (such as metal nitrides, hydrides, oxides, borides, etc.); transparent conducting oxides; and dielectrics [55].

Nevertheless, all Metasurface-based devices can be classified as broadband, wideband, and narrowband according to their frequency responses [54]. As shown in Figure 2.2 all Metasurfaces can be divided into two general classes Plasmonic and dielectric Metasurfaces [56].

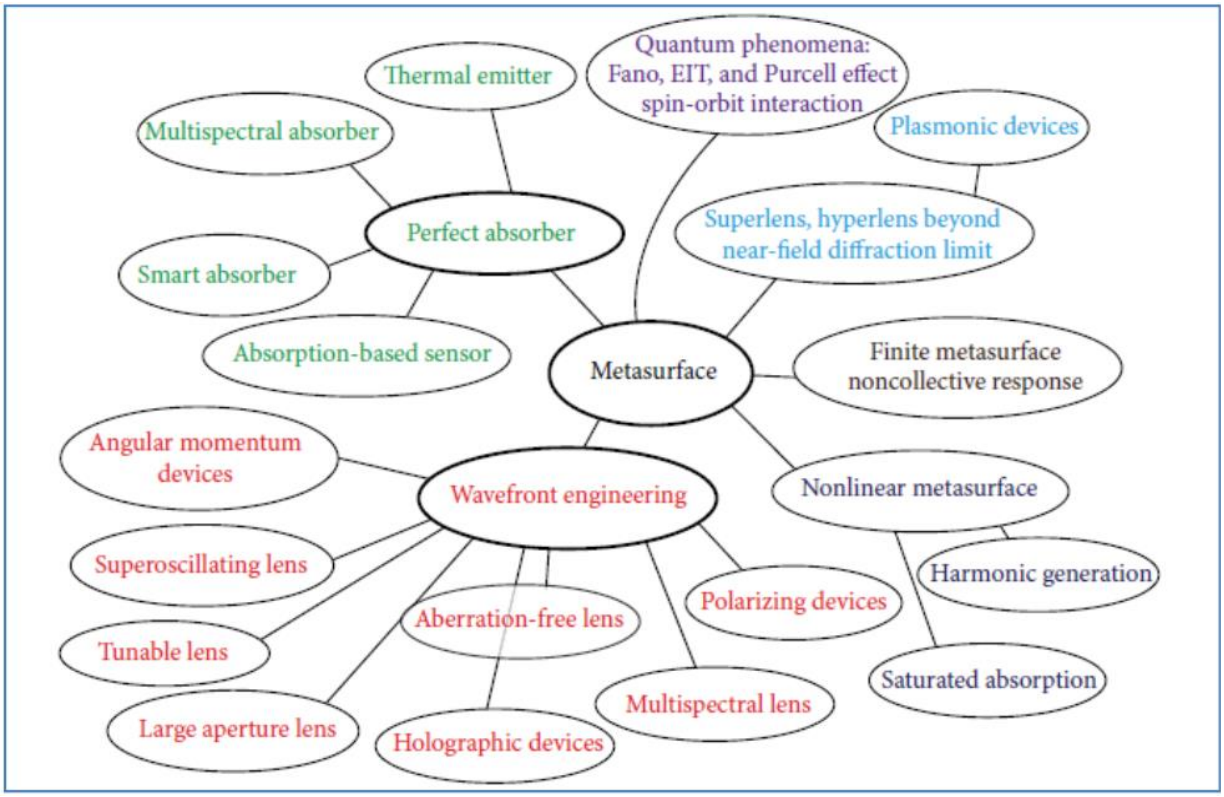

Figure 2. 3: Outlook of the future trends of Metasurface and meta-devices applications [57].

As illustrated in Figure 2.3 , in the upcoming few years, the researches in Meta-surfaces will be focused on aspects including but not limited [57].In a general way, there is an obvious trend for extending the researching frequency regime from microwaves to the optical regime or the new emerging THz region. One may wonder that the extension of the frequency range is straight forward, and thus not so physically meaningful. Therefore, we must bear in mind that the properties of the materials itself would change dramatically at different frequencies. The measurement equipment and the fabrication techniques will also vary..At optical frequencies [58], even quantum phenomena would play an important role.

A Plasmon is a quantum of free electrons oscillation. Free electrons clouds in a metal can couple to light at an interface between metals and dielectrics media and can create surface plasmons, it can deal with the coupling between the electronic oscillations and the electromagnetic field of material. With adequately designed nanostructure made from metal,

the surface plasmons can make it possible to control the light at the sub-diffraction scale. Not only the plasmonic nanostructures can guide light at the nanoscale, but also they can increase the local intensity of an electromagnetic-field by orders of magnitude [59].

For the metallic subwavelength structures or nanoparticles, the electric-field of incoming radiation polarize the conduction electrons. The resulting plasmon oscillations are distributed over the nanoparticle volume and they are localized within the particle. These plasmon oscillations are termed localized surface plasmons (L.S.P.s). The displacement of the electron clouds from the lattice generates a restoring force that tries to pull the electrons back into the lattice. Therefore, the nanoparticles act as an oscillator driven by the incoming field together with restoring the Coulomb force and behaves as a simple dipole in directions of the electric field. When the frequency matches the resonance, frequency defined by the shape of the particle, (L.S.P) resonance occurs, enhancing local field amplitude. The nanostructure can introduce also a local phase shift for the incoming light beam and manipulates the wavefront [56].

Despite all the promising applications for plasmonic Meta-surfaces, optical losses in plasmonic devices severely limit their use in replacing the conventional optical elements. As electron-clouds in the metal oscillates while interacting with the incoming electromagnetic waves, they experience a scattering in the materials that causes heat generation. Even though for the best plasmonic material, low loss or we can say small imaginary part of permittivity and high plasmonic property which is a large negative real part of permittivity are essential, the losses cannot be avoided completely. Even for a perfect plasmonic material with negligible loss, Nanostructuring the metal causes the magnetic field of an incoming electromagnetic wave to be truncated as the wave interacts with the free-electrons of the structures. Also, the material has a different platform as it is shown in table 2.2.

Material type	Examples	Wavelength range	Advantages	Limitations/challenges	Application examples
Plasmonic metal	Au, Ag, Al, Cu...	Visible–mid IR	- Established fabrication - Plasmonic in the UV part of the spectrum (Ag, Al) - Biocompatible (Au) - Small device footprint - High field concentration	- Relatively low melting point; - Lack of tunability - High solubility/diffusion at elevated temperature - Low chemical stability (Ag, Al)	- Proof-of-concept demonstrations of compact and flat optical devices - Biosensing (Au) - Structured coloration and holography (Al)
Refractory	TiN, ZrN, HfN, W, Ta…	Visible–mid IR	-High durability -High melting point -CMOS compatible -Chemical stability (TiN) -Biocompatible (TiN) -Low solubility -Epitaxially grown -Possibility of growing ultrathin films (few nm)	-Higher optical loss in visible compared to noble metals -Strict fabrication requirements	-Local heating and absorbers -High temperature and high intensities -Fabrication of epitaxial Ag (TiN) -Biomedical thermoplasmonics (TiN)
2D	Graphene, MXene, phorsphorene, MoS2, WSe2, WS2…	Visible–mid IR	-Dynamic tunability (electrical) -Fast modulation -Large field confinement -Compactness/lightweight -Mechanical flexibility -Lower loss than noble metals in near IR	Poor light absorption with single layer	Dynamically tunable and flexible devices
Phase change	GST, VO2, YH2, MgH2, PdH2, SmNiO3	Visible–mid IR	-Dynamic tenability (temperature) -Large optical modulation	Relatively slow modulation	Nonvolatile reversible optical switches
Transparent conducting oxides	ITO, Ga:ZnO, Al:ZnO	Visible–mid IR	-ENZ in near IR -Ultrafast tenability (optical, electrical, temperature)	Less plasmonic in the NIR compared to noble metals	Ultrafast optical modulators
Dielectric	Si, TiO2, SiO2, Si3N4, diamond	Visible–Near IR	Very low-optical loss chemical robustness and Mechanical	Larger device footprint Low field confinement	Highly efficient metasurfaces

Table 2. 2: Different material platforms with their wavelength range, advantages, limitations and applications[56]

2.5.1. Dielectric metamaterials

Since the onset of the successful demonstration of light-bending at the ultrathin scale reported by Refs [60] and [61], the plasmonic Meta-surfaces field has rapidly grown due to the compactness and high optical confinement, also the efficient hot electron generation found in the systems. As we discussed in the previous section plasmonic Meta-surfaces suffer from optical losses because of strong(electron-electron) and (electron-phonon) scattering in metals, which can limit the main efficiency of a functional optical device such as (lenses, holograms, spectrometers, wave plates, etc) [62]. The mission for highly efficient planar optical manipulators has guided and let to the development of all-dielectric Meta-surfaces. Unlike plasmonic Meta-surfaces, which relies on L.S.P resonances to realize their features, dielectric Meta-surfaces are based on the collective light-scattering it's also known as Mie scattering of the constituent high index dielectric nanoparticles with dimensions comparable to the wavelength of light inside the particles [63], [64]. Optical loss can be minimized in all-dielectric Meta-surfaces as the large bandgap energies in dielectric materials limit optically induced inter-band transitions. Therefore, when light (with sub-bandgap energies) impinges upon dielectric nanoparticles, no free charge carriers are available, and only displacement currents instead of conduction currents are induced. This results almost in negligible optical losses and high electric field concentration inside dielectric nanoparticles, in contrast to metallic nanoparticles where a significant portion of the incident optical energy converts to heat and strong electric field concentration happens close to surface outside the nanoparticles. While it might be not surprising that all dielectric Meta-surfaces outperforms metallic Meta-surfaces in transmission applications since metal's exhibit large optical reflection and the absorption, even in reflectors where metals find the most efficient applications [65], [66].

Experimentally demonstrated all-dielectric near perfect (99.8%) reflectors outperform metallic mirrors inefficiency which experience (~2%) intrinsic loss notified by [65] and [66]. The possibility to engineer both magnetic and electric resonances in dielectric nanoparticles endows all-dielectric Meta-surfaces with functionalities unattainable in their plasmonics counterparts. Dielectric Meta-surfaces are normally constructed by periodic or another deterministic arrangement of high index sub-wavelength dielectric scatterers. However, they shouldn't be confused with photonic crystals because they are also made as periodic arrays of scatterers. The dielectric Meta-surfaces function relies on the collective optical response of individual constituent's building blocks to form the desired wavefront in the far-field.

2.6. Selective metamaterial emitters for TPV systems

2.6.1. Selective emitter requirements

A selective emitter with high performance may have, either broadband absorption with a selective emission, where any in-band photons are preferentially emitted, correspond to energy greater or wavelength below TPV cell bandgap, where E_g and λ_g are the bandgap energy and wavelength, respectively, or narrowband emission, where the photons with energy slightly above the bandgap are emitted, This is illustrated in Figure 2.4 (a). Note that we refer to photons or radiation both in energy terms and wavelength. Figure 2.4 (b) shows the goal of angular control is to ensure good spectral control (preferential in-band emission) over a wide range of angles, as thermal radiation can be off-normal. Figure 2.4 (c) illustrates the view factor loss, where photons are lost through the emitter-TPV cell gap, is a significant source of loss [67].

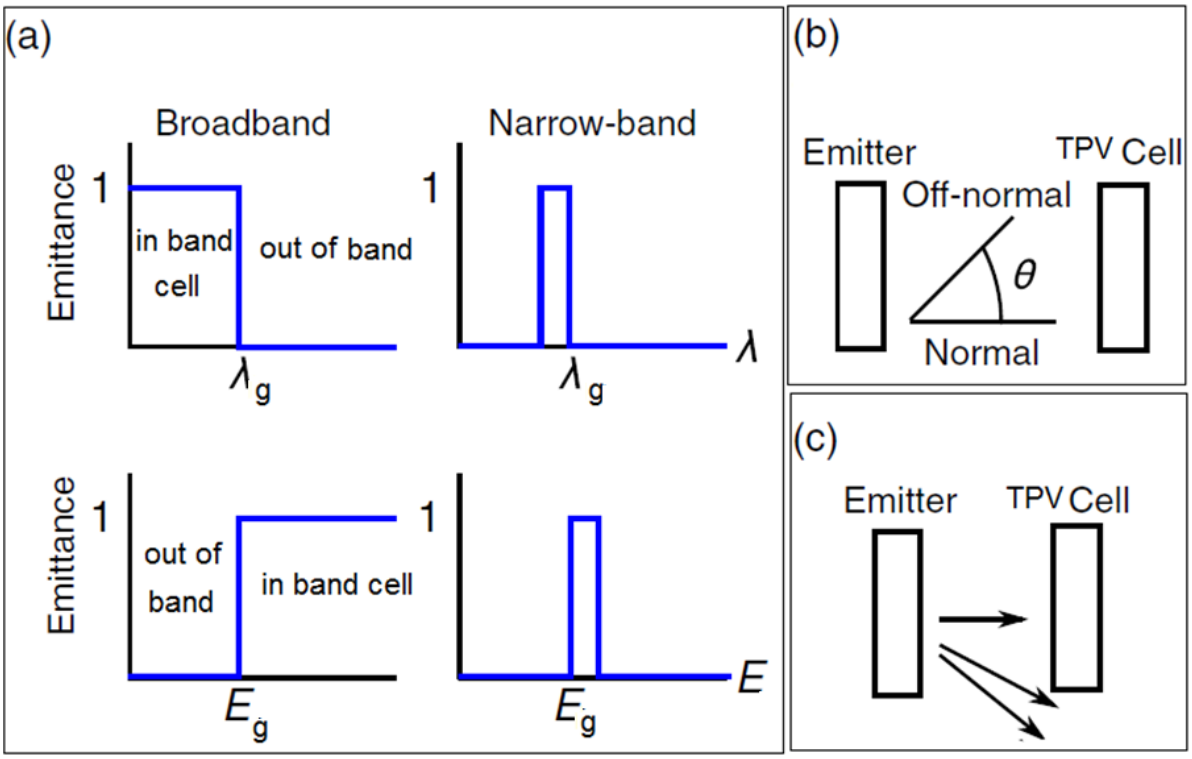

Figure 2. 4: An emitter with high performance may have (a) Ideal spectral control. (b) Angular power emission of thermal radiation. (c) View factor loss[67]

Although an emitter with cold side filters performs better than a direct blackbody excitation, relatively higher temperature and mitigated TPV cell efficiency reduction, and it suffers from view factor also absorption losses. In a view of factor loss, which it's inherent to the systems with the diffuse emitter, Figure 2.4 (c) shows the photons lost in the finite gap that is between the emitter and the cell. However, it is possible to reduce the factor loss by reducing emitter area relative to the cell area, keeping an emitter arbitrarily small decreases the absolute radiated power [67]

2.6.2. Design Methodology

The basic methodology of our study will include the following steps: characterizing the relevant materials already used for TPV cells and possibly new materials, including the optical proprieties of the materials needed for the calculations as well as the numerical simulation of the spectral absorption as well the emissivity of a new the suggested design structure and it's based on finite element method (FEM) approach which is integrated into the full-wave solver (HFSS). These calculations will be implemented in a MATLAB program model to analyze the new TPV designs and potentially find efficient designs for different TPV cells and their EQE-spectrum. The methodology of our study is summarized in figure 2.5.

The fast development and compact combination of both computer technology and also simulation technology within different researches fields, the selection of the proper simulation tool can improve the accuracy and efficiency during the process of simulation analysis. As optical energy, it's a wave composed from coupled electric and magnetic fields oscillating in synchrony at hyper-frequencies, the analysis of optical MMs can be changed to the analysis of the interaction between electromagnetic and matter.

HFSS ANSYS software is the industry-standard simulation tool for 3D full-wave electromagnetic field simulator and it's essential for the design of high frequencies and high-speed components. HFSS offers you multiple states of the art solver technologies and it's based on the proven FEM or the well-established integral equations method depending on the simulation type. This solver is based on a really powerful automated solution process, the user is required to specify only the geometry and material properties and the desired output. From this information, HFSS automatically does generate an appropriate, efficient, and accurate mesh for solving the problems using the selected solution technology. ANSYS HFSS is

electromagnetic analysis software that is based on frequency-domain analysis technology. As a result of this characteristic, HFSS suites more for studying an object in a narrow bandwidth.

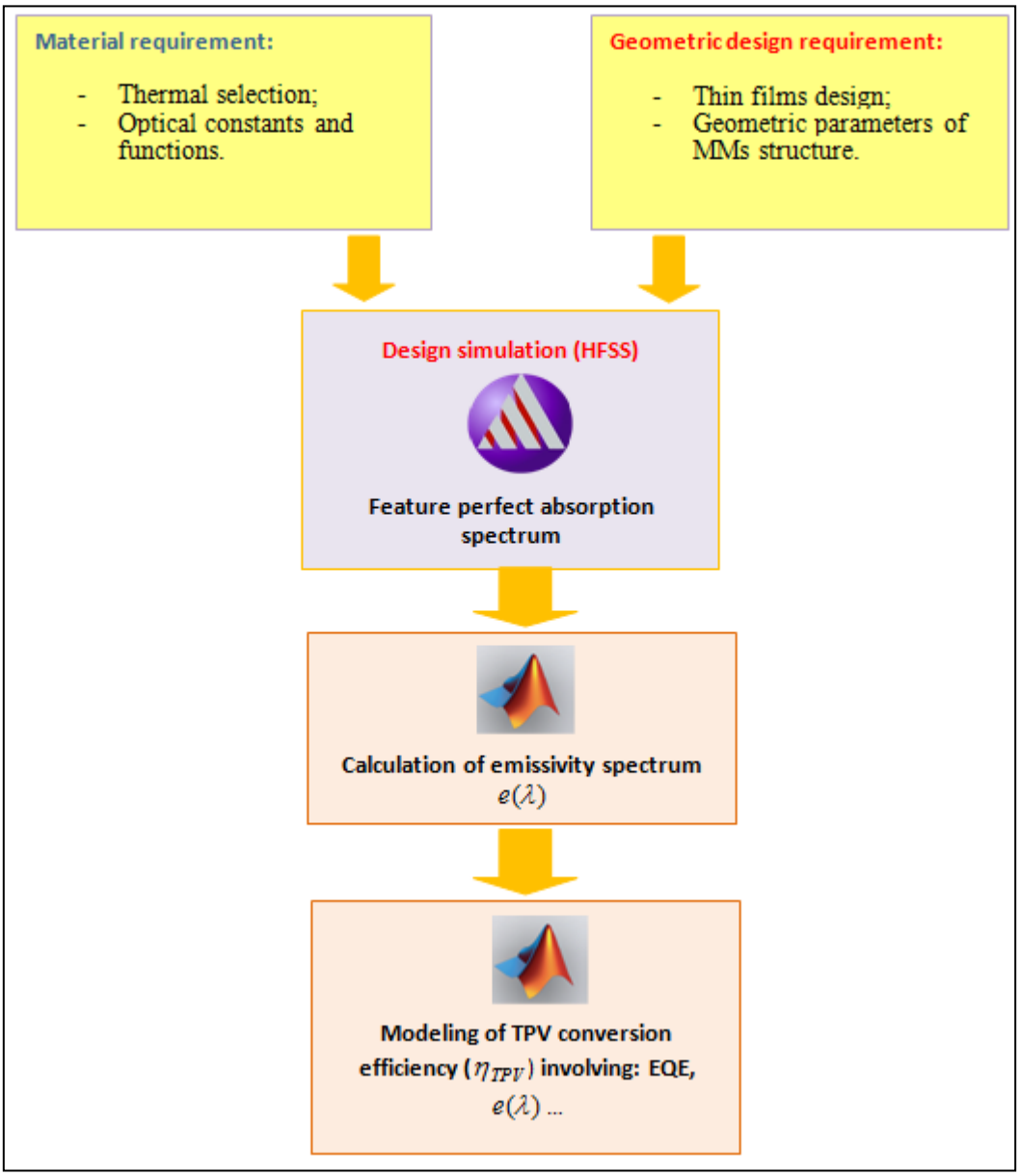

Figure 2. 5 : The methodology of modeling the new design of TPV conversion system

2.7. Conclusion

In this thesis that set out to make a theory of electromagnetic MMS and a brief historical review explaining involving MMS idea in different domains particularly in developing absorber/emitter, a better understanding of MMS needs basics of electromagnetic properties that were explained in both cases dielectrics and metals put an appearance of plasmonics that were discussed alongside with all the emitter/absorber requirements. In conclusion, we offered a design methodology to study and characterize the relevant materials already used for TPV cells based on (FEM) which is integrated into (HFSS) side to side with MATLAB.

Chapter 3: Simulation of a new design of the TPV system

3.1. Introduction

In this chapter, we will define the 3D simulator (HFSS) and the mathematic approach for better understanding of the main limitation compared to the experimentally. Afterward, we will elaborate the absorption and reflection spectra in different polarization and incident angle sensibility, and all simulation outcome will be amended for adequate shape for selected external quantum efficiency (EQE), then we will investigate the emissivity spectra to reach the maximum TPV efficiency possible in different temperatures either by lowering the bandgap or making the opposite. In such cases, we will compare the thermophotovoltaic efficiency of some commonly used solar cells.

3.2. Simulation tools

To modeling electromagnetic MMs structures, several methods are available, such as plane-wave expansion and spherical-wave expansion (PWEM), finite-difference time-domain (FDTD) method, transfer-matrix method (TMM), finite-element method (FEM), method of moment (MoM), and others. Generally, the computational electromagnetic approaches can be classified into either frequency-domain simulation, or time-domain simulation [68]. Each category can be auxiliary classified into two dimension-based (2D), or three dimension-based (3D) methods.

There exist several of commercially available software that can easily deal with analysis and simulation of MMs and associated structures as well as general periodic structures, such as High-Frequency Structure Simulation (HFSS) by ANSYS based on FEM method solver, with helpful adaptive mesh refinement, and integrated electromagnetic simulation software (IE3D) by Zeeland software, with the software package (FEKO) The name is derived from the German acronym "FEldberechnungfür Körpermitbeliebiger Oberfläche", which are based on moment method, and the computer simulation technology CST MICROWAVE STUDIO which is based on FDTD approach, and multi-physics COMSOL based on FEM. Whereas, for generalized 3D structures on needs to use a FEM or FDTD approaches [53]. There is a varying rate of accuracy depending on the mesh resolution that is normally traded off against the computational time of the simulation.

In this work, we select the FEM approach which is represented by the software HFSS solver offered by ANSYS [69]. The basic classical losses of the model are employed (by default) with being moved into the material setup and dialog box. on the other hand, the simple relaxation model effect can be used by infiltrating data files containing a non-complex (a real notation forms) conductivity values calculated a priori for each discrete frequency point [7].

To make the simulation faster, you can just replace solid metal walls by boundaries. Frequency dispersion models can also be used in the material parameters for 3D design (referring to solid object) or boundary condition, with the former, the use of bulk meshing is dependent on the threshold value of conductivity (for HFSS this is 10^5 S/m, by default).

The Finite Element Method (FEM) is one of the originally more complex and universal methods, it's used for such a problem is a frequency-domain method, which is based on Maxwell's equations. To solve a given frequency, a system of linear equations needs to be solved. The large matrix inversions required can result in substantial computational requirements.

This approach is a numerical process to find accurate and stable solutions to boundary-value partial differential equations the first time reported in 1943 by Richard Courant in his work of elasticity and structural analysis [70], where the concept of mesh procedure of simulation was introduced. It was not until 1969 that the method was introduced to the field of electromagnetic engineering after Silvester used this approach in the field of microwave engineering [71]. FEM assumes that the resonant structure is surrounded by an artificial absorbing boundary condition which approximates the electric and magnetic fields approaching zero at infinity:

$$\hat{n}\times(\nabla\times E)-ik_0\hat{n}\times\hat{n}\times E\approx 0 \tag{3.1}$$

$$\hat{n}\times(\nabla\times H)-ik_0\hat{n}\times\hat{n}\times H\approx 0 \tag{3.2}$$

where $\hat{n}$ represents the vector normal to the boundary surface and k_0 is the incident free-space wave vector [72], as the boundary conditions in equations (3.1) and (3.2) are combined with the vector wave equation for the electric field of Maxwell's equations:

$$\nabla \times (\frac{\mu_0}{\mu_{ij}}.\nabla \times E) - k_0^2 \varepsilon_{ij} E = -ik_0 \sqrt{\frac{\mu_0}{\varepsilon_0}} J - \nabla \times \frac{\mu_0}{\mu_{ij}}.M \tag{3.3}$$

where *M, J* are the magnetic and electric current density, respectively, and the anisotropic materials permittivity (ε_{ij}) and permeability (μ_{ij}) of the structure under consideration, we obtain:

$$\begin{aligned} &\iiint_V \left[(\nabla \times T).\frac{\mu_0}{\mu_{ij}}.(\nabla \times E) - k_0^2 T.\varepsilon_{ij}.E \right] dV = \\ &\oiint_{S_B \cup S_{surf}} \hat{n}.\left[(T \times \frac{\mu_0}{\mu_{ij}}.\nabla \times E) \right] dS - \iiint_V T.ik_0 \left[\sqrt{\frac{\mu_0}{\varepsilon_0}}.J + \nabla \left(\frac{\mu_0}{\mu_{ij}}.M \right) \right] dV \end{aligned} \tag{3.4}$$

where *V* depicted the total volume of integration, S_B is the artificial absorbing boundary surface, S_{surf} is the surface of the structure being simulated, and T is an appropriate test function used for integration convergence. The combining of the latest four equations offers:

$$\begin{aligned} &\iiint_V \left[(\nabla \times T).\frac{\mu_0}{\mu_{ij}}.(\nabla \times E) - k_0^2 T.\varepsilon_{ij}.E \right] dV = \\ &\oiint_{S_{surf}} (\hat{n} \times T).\frac{\mu_0}{\mu_{ij}}.(\nabla \times E)\ dS - ik_0 \oiint_{S_B} (\hat{n} \times T).(\hat{n} \times E)\ dS - \\ &\iiint_V T.\left[ik_0 \sqrt{\frac{\mu_0}{\varepsilon_0}} J + \nabla \times (\frac{\mu_0}{\mu_{ij}}.M) \right] dV. \end{aligned} \tag{3.5}$$

The volume *V* is then meshed into sub-regions using trapezoidal, tetrahedral, or other types of meshing formats, where the conformal nature of these meshes is especially useful with curvature surfaces. To get a solution to the electromagnetic problem suggested in equation (3.5), the E-field tangent to each edge of an individual meshing cell is calculated, and a set of basis vectors are used to extrapolate the resulting fields throughout the remaining simulation volume. The E-field within the entire structure is then given by:

$$E = \sum_{k=1}^{R_{\max}} R_k E_k \tag{3.6}$$

where R is the vector field component along a given meshing cell edge, $R_{\max}$ is the total number of edges within the simulation except for S_{surf}, and E_k is the tangential electric field component along the same edge. When the basis vectors, R are the same as those in the test function T, we can combine equations (3.5) and (3.6) to find the discretized, Galerkin formulation of the electromagnetic problem for a single frequency:

$$\sum_{k=1}^{R_{\max}} M_{kh} E_k = -\iiint_V R_h . \left[ik_0 \sqrt{\frac{\mu_0}{\varepsilon_0}} J + \nabla \times \left(\frac{\mu_0}{\mu_{ij}} . M \right) \right] dV \tag{3.7}$$

where M_{kh} is given by:

$$M_{kh} = \iiint_V \left[(\nabla \times R_h) . \frac{\mu_0}{\mu_{ij}} . (\nabla \times R_k) - k_0^2 R_h . \varepsilon_{ij} R_k \right] dV - ik_0 \oiint_{S_B} (\hat{n} \times R_h) . (\hat{n} \times R_k) \, dS \tag{3.8}$$

The results of such computational software solver are usually the distribution of electromagnetic waves, which should be processed using the retrieval algorithm to extract the scattering parameters (S) of the designed structures. On this basis, we hold that by using FEM approach we will be able to predict the performance of MMs-based THz components with more confidence and converged results compared to the experimental.

3.3. Design of metamaterial absorber/emitter

Figure 3.1 shows the schematic of new MMs emitter from a different viewpoint, it has been suggested and experimentally confirmed in a new study offered by Sakurai et al from Niigata University (Japan) [73]. A periodic metallic disk patterned on a dielectric film, which is placed on top of a metallic film, respectively. Silicon dioxide (S_iO_2) was chosen as a dielectric spacer and Tungsten (W) was chosen as the metallic part of the proposed absorber/emitter MMs device, however, the interesting part of (W) particularly the melting point (3422 °C) hence, Therefore, we assumed that proposed MMs-structured was reasonable, to be utilized, for the TPV emitter applications, which requires a high operating temperature.

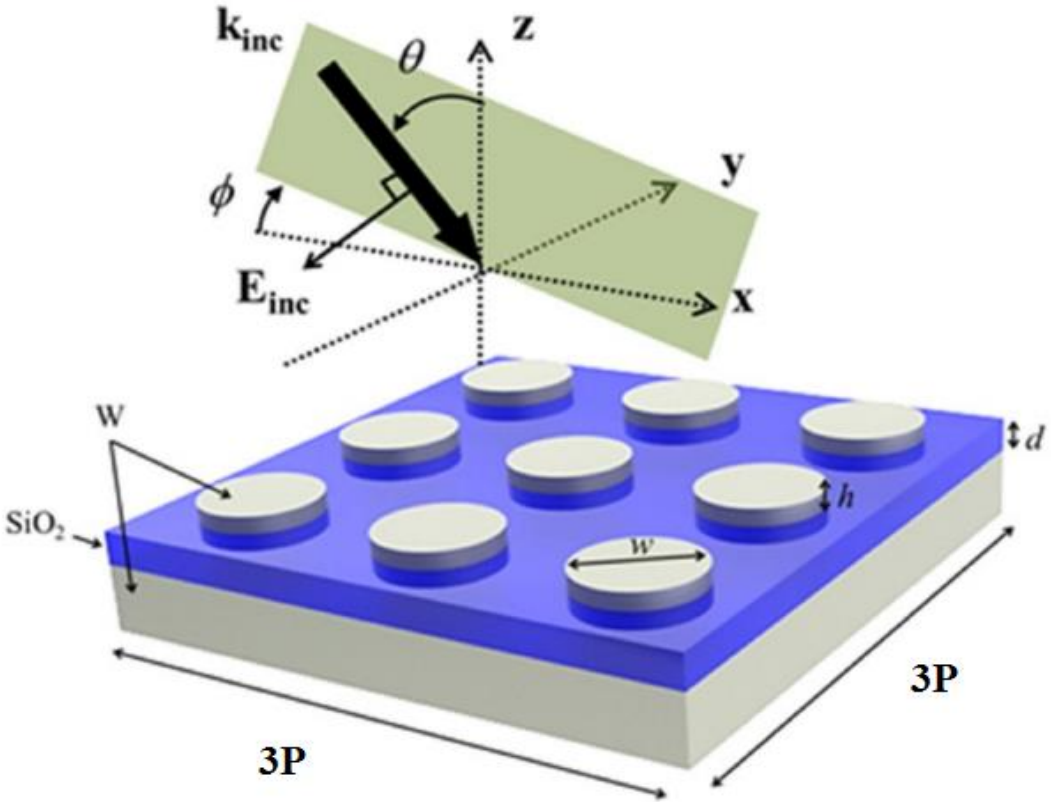

Figure 3. 1: 3D view of the proposed MMs absorber/emitter design*[73]*.

The geometric parameters of this absorber/emitter are given as, the diameter of the disk *w*=350nm, with a thickness of *h*=50 nm, S_iO_2 thickness is *d* =100 nm. Periods of the unit cell

for the *x* and *y* directions were P=600 nm. The dielectric function of W can be described by an adapted expression of the Drude model in the terahertz domain as [74]:

$$\varepsilon(\omega) = 1 - \frac{\omega_p^2}{\omega.(\omega - i\omega_c)} \tag{3.9}$$

where plasma frequency is $\omega_P = 1448$ THz and the collision frequency $\omega_c = 13$ THz [75]. The dielectric functions of S_iO_2 spacer were obtained from the tabulated data from Palik [76]. θ And ϕ represent the incident and polarization angles of the incident light, respectively.

3.3.1. Absorption spectra

Figure 3.2 represents the simulated spectral absorption (blue dashed line) compared to the measured spectral of the fabricated MMs absorber/emitter (red dots). We can observe two peaks at $\lambda_1 = 0.81\,\mu$m and $\lambda_2 = 1.59\,\mu$m with an absorption rate of 98.3% and 99.8%, respectively. The bandwidth of absorption can be extended from 0.5µm to 2.5µm.

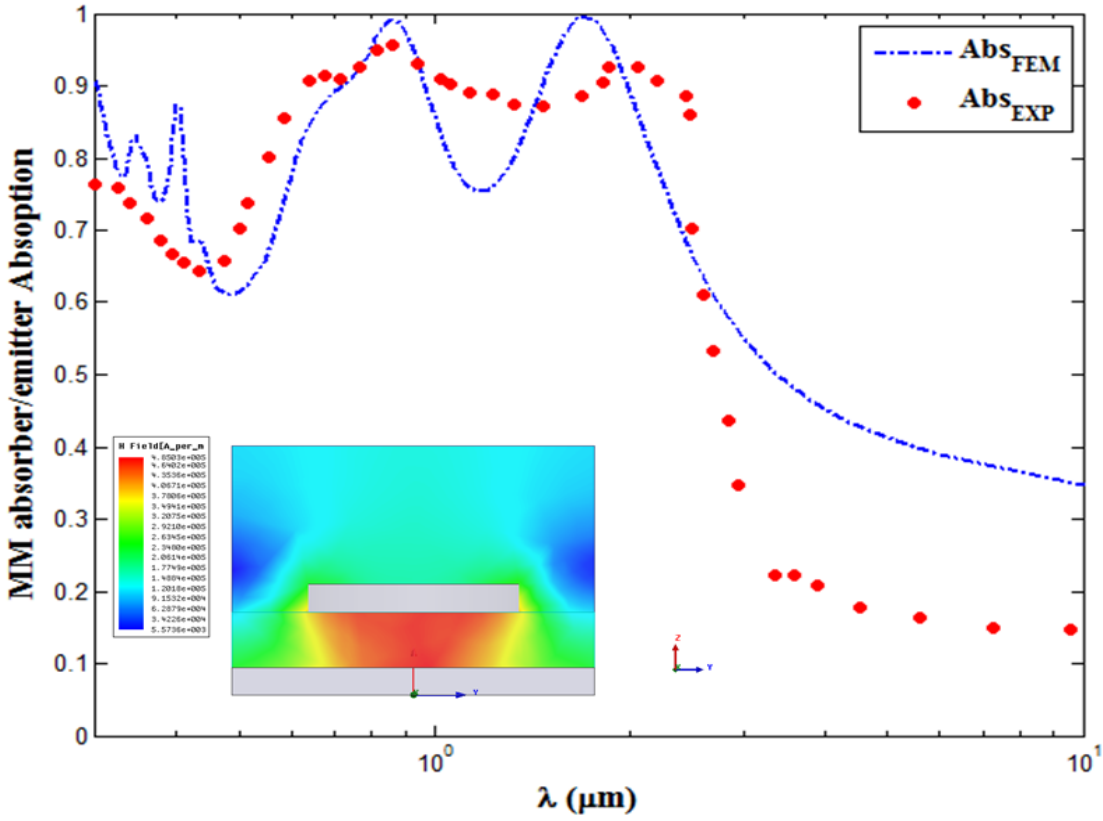

Figure 3. 2 :Simulated absorption for the new designed MM absorber/emitter, compared to the experimental results *[73]*.

The measured absorption showed reasonable agreement with the numerical absorption simulated by FEM approach. However, there was an absorption mismatch at the wavelength shorter than the larger wavelength. The diameters of the W disks were patterned slightly larger than as designed from the simulation [73], as well as the theoretical simplification model of optical losses can be offered by HFSS solver, generally, these were the reasons why the absorption spectra shape was shifted.

Since the proposed MM absorber/emitter, magnetic polariton (MP) could be excited in the dielectric spacer between the metals [77], [78]. As well, figure 3.2 depicts the magnitude of the y-component magnetic field, and at the peak wavelength, highly localized y-component magnetic field enhancement can be observed in the S_iO_2 film between the W disk and the

bottom W plate. Furthermore, the electric field created a closed current loop, which created an enhanced magnetic field and thus formed MP. Therefore, the proposed absorber/emitter (which excites MP) could be said to have a strong emissivity peak at the highest EQE wavelength region of the commonly used TPV cells (e.g. GaSb, InAsSbP...), more detail in the next section.

This absorption is a result of an impedance adaptation between the effective impedance of MTM structure $Z_{eff}(\omega)$ and free space impedance $Z_0(\omega)$ [74] :

$$Z_{eff}(\omega) = Z_0(\omega) \tag{3.10}$$

$$Z_0(\omega) = \sqrt{\frac{\mu_0}{\varepsilon_0}} \tag{3.11}$$

$$Z_{eff}(\omega) = \sqrt{\frac{\mu_{eff}(\omega)}{\varepsilon_{eff}(\omega)}} \tag{3.12}$$

This happens by carefully toiling MM structure geometric parameters which lead to alteration of both effective electric permittivity $\varepsilon_{eff}(\omega)$ and effective magnetic permeability $\mu_{eff}(\omega)$ of the MTM structure [74] :

3.3.2. Polarization and incident angle sensibility

As a MM absorber is based on a periodic array of resonators, it operates at a specific frequency and has a narrow-bandwidth. Studies on increasing the bandwidth of the MM absorbers have been reported over the past years. In general, the absorption of an MM absorber/emitter is also dependent on the incident angle and the polarization. Polarization-insensitive MM absorbers can be achieved by designing a horizontally and vertically symmetric unit cell [79], [80].

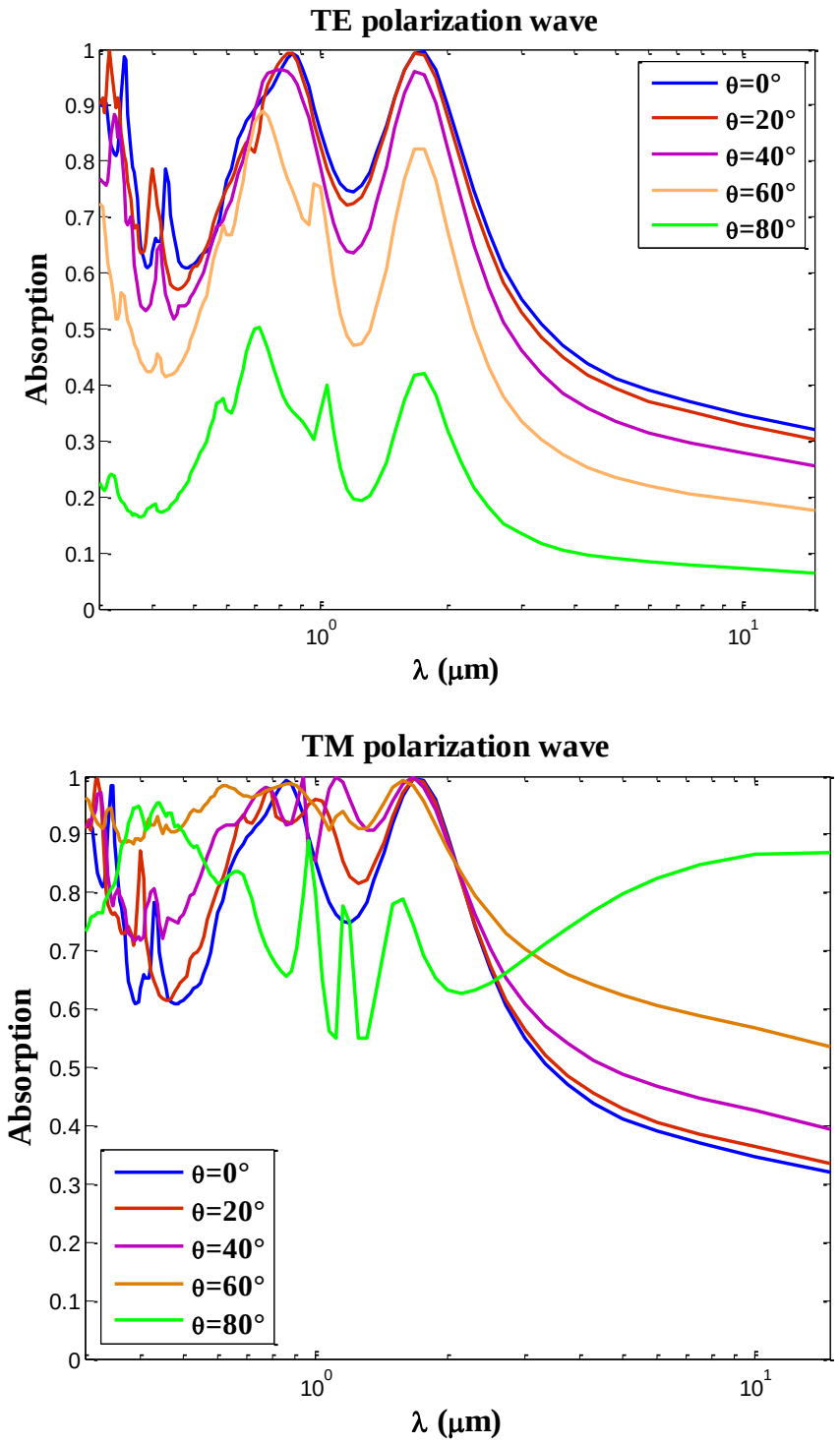

Figure 3. 3: Absorption effect of different angles of incidence for TE and TM polarization wave.

In the suggested absorber/emitter structure, the results for different incidence angles are shown in Figure.3.3 as for TE polarization; the largest incidence angle can reach 70° when the

minimal absorption rate remains more than 0.85. For TM polarization wave, the largest incidence angle can be reached is 80°.

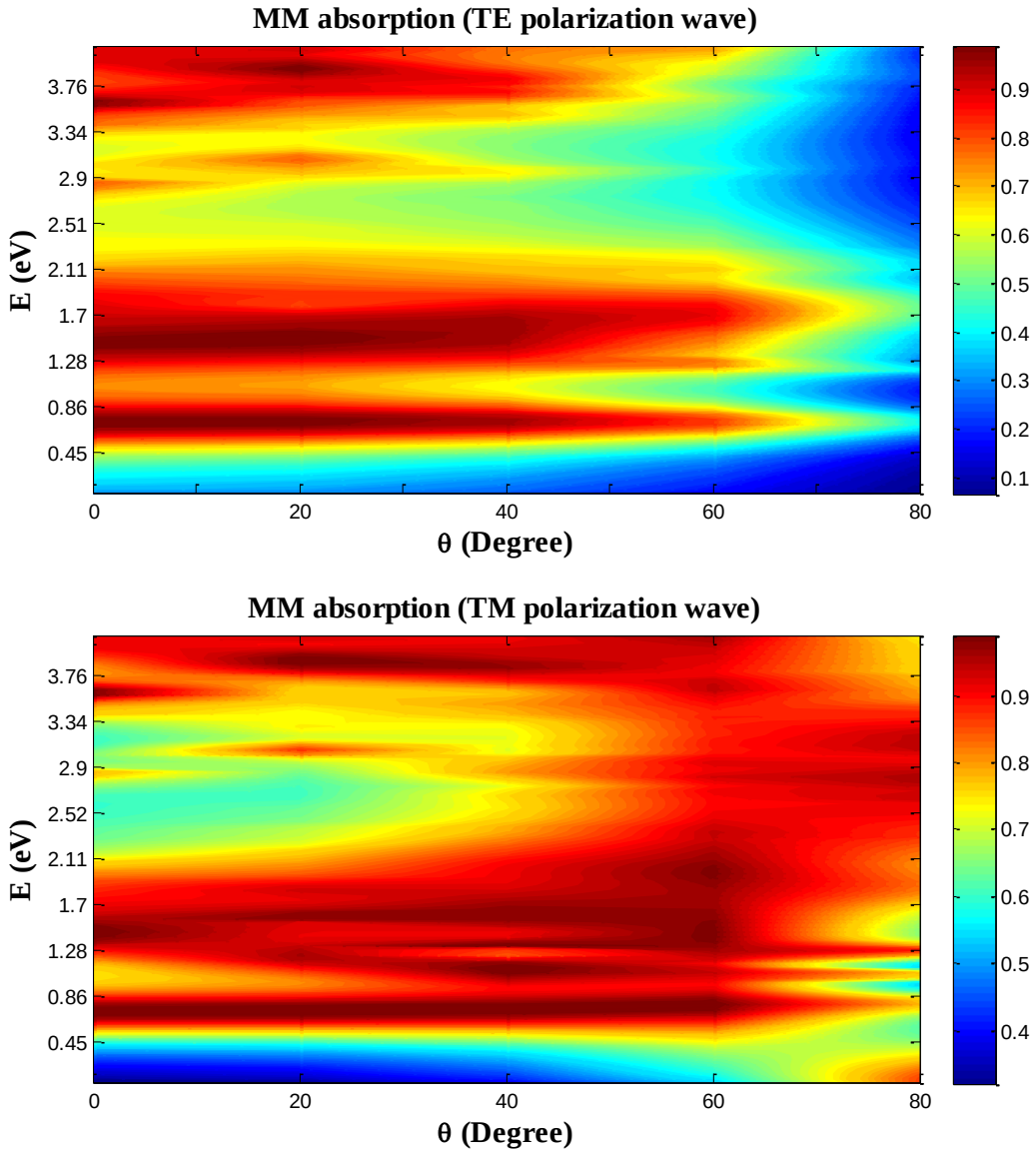

Figure 3. 4: Diagram of dispersion for absorbed energy by different incidence angles for a TE and TM polarization wave.

Furthermore, the absorption is simulated as a function of frequency and incident angle in Figure.3.4 to examine the angle dependence of this absorber/emitter. the perfect absorption rate is insensitive to the incident angle for TE and TM polarizations, and the minimal absorption magnitude from 0.45 to 1.7 eV is larger than 0.80 for angles up to 70° for different

polarizations. Therefore, the present broadband absorber can operate in a wide-angle range. The strong absorption rate is due to the coupling of the magnetic resonance inside a micro/nanostructure with the external electromagnetic waves or magnetic Plasmon polariton. When the magnetic polaritons are excited, the magnetic field is strongly enhanced in the dielectric layer inserted between the tungsten disk and tungsten substrate as shown in figure 3.2 of absorption.

3.3.3. Emissivity spectra

To reach high TPV efficiency, MMs absorber/emitter component can be introduced between the heat source and the TPV cell. This device should be a perfect selective thermal emitter having high emissivity regions of high external quantum efficiency (EQE) of TPV sub-cell and low emissivity for other spectral regions. The MM absorption $A(\lambda)$ is utilized for achieving spectrally selective thermal emissivity, by Kirchhoff's law: $e(\lambda) = A(\lambda) \times e_{BB}(\lambda, T)$, where $e_{BB}(\lambda, T)$ is the blackbody emissivity spectrum at temperature T.

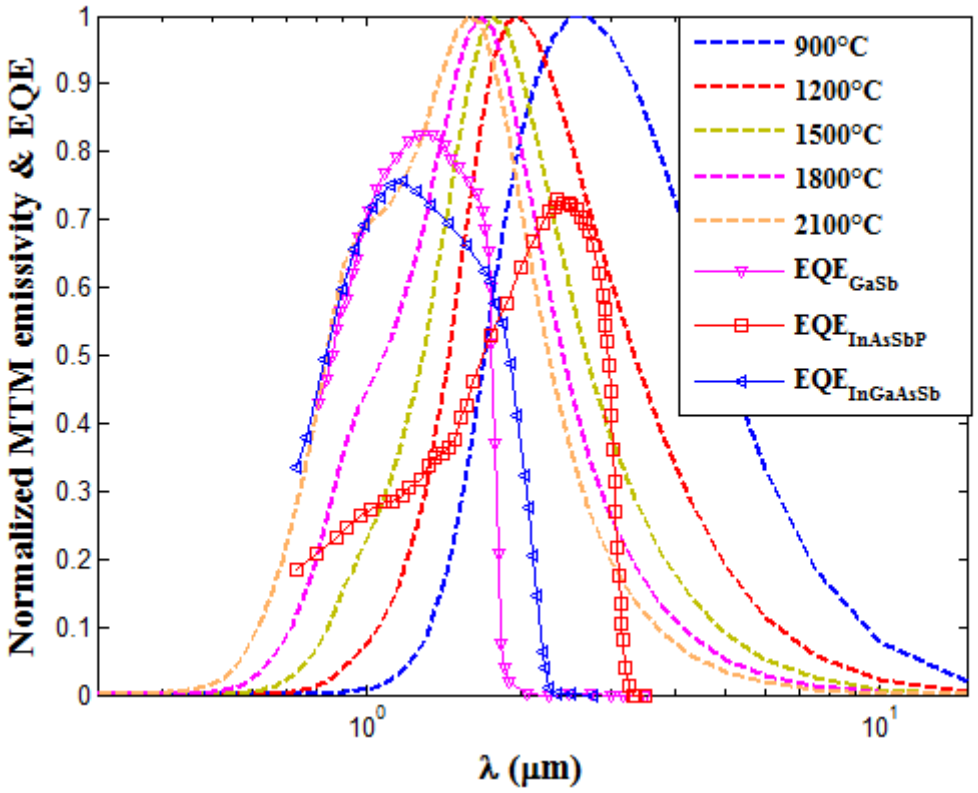

Figure 3. 5 :Simulated emissivity spectra of the new absorber/emitter for different temperatures compared with commonly used EQEs TPV cells [81].

Figure 3.3 represents the spectral emissivity calculated from the absorption spectra obtained from HFSS software, for different operating temperatures from 900 to 2100°C, and EQE of each commonly used TPV cells, in order, for a best correlate with the best emissivity. We observe for low-temperature cases (<1500°C), the MM emissivity spectrum is adequate for InAsSbP TPV cell with E_g=0.37eV correspond to the wavelength of 3.28μm, on the other hand, InGaAsSb and GaSb cells exhibit a suitable EQE at high temperatures (1900-2100 C°). Each cell is assumed to absorb all the photons with energies larger than the bandgap of the cells. In such a case the absorption of incident photons having energy lower than bandgap leads to thermal leakage and causes TPV system inefficiency due to the mismatch between the emitter radiation spectrum and the EQEs of recommended TPV cells.

3.3.4. TPV system efficiency

To reach high efficiency, an intermediate absorber/emitter can be introduced between the heat source and the cell, is shown in Figure.3.6. The intermediate device should be a perfect selective thermal emitter having high emissivity regions of high external quantum efficiency (EQE) of TPV cell and low emissivity for other spectral regions. Tuning the radiated power bandwidth emission, to match the TPV cell band-gap enhances the power conversion efficiency of the cell. Incident photons with energy lower than energy bandgap (Eg) are not useful and go off as thermal loss with lowered efficiency, thus to reach maximum efficiency we need to match the best performed (EQE) spectra of TPV cell.

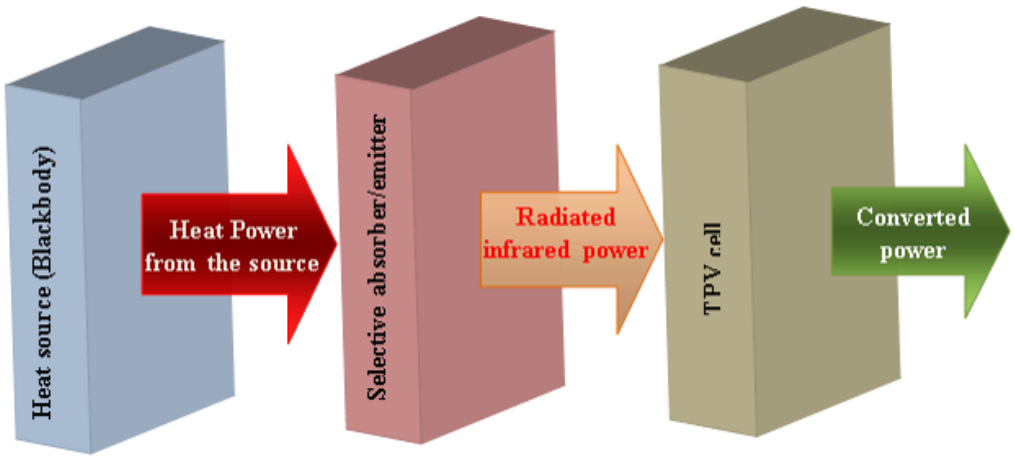

Figure 3. 6: Thermophotovoltaic system based on combined PV cells with the selective MM absorber/emitter design.

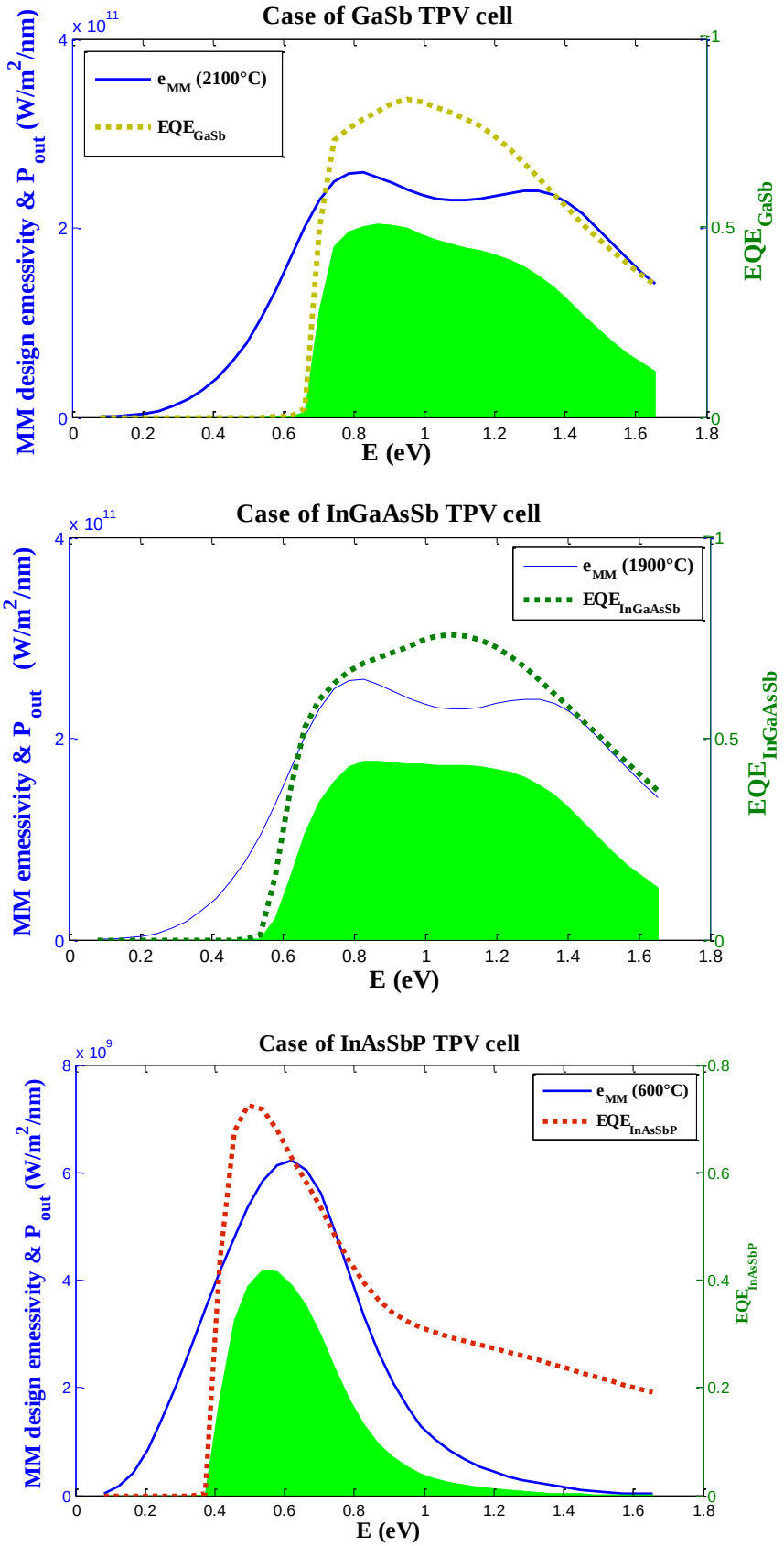

Figure 3. 7: the emissivity spectra and EQE are plotted with the output power density exhibited by commonly used cells.

The emissivities of a typical absorber/emitter design are shown by the blue solid line in Figure 3.7. The dashed line denotes EQE of GaSb, InGaAsSb, and InAaSbP cells, which can exhibit a peak up of 86%, 80 %, and 75%, respectively. The green areas are the maximum outcome powers and it represents all absorbed incident density photons, the absorber/emitter temperature has a critical role as it decides for the overall efficiency. The design considered in this study is suitable for the TPV system consisting of GaSb-based cells. GaSb efficiently generates electricity only if it's in the range of (0.66 eV to 1.64eV) of incident falling photons for an operating temperature of 2100°C.

Furthermore, the case of InGaAsSb shows slight differences in the absorption energy of incident photons as illustrated with GaSb, the optimal conversion can be reached under the operating temperature of 1900°C. Another hand, for InAaSbP is favorably centered the emissivity at E=0.38eV which correspond to a working temperature of 600°C, the incident photons with energy lower than energy Eg are not useful and go off as thermal loss with lowered efficiency, thus at the low-temperature range we head up less band-gap followed by decreasing in power output, P_{out} and it depends on the density of photons having higher energy than TPV cell energy band-gap, as shown in the following equation [82]:

$$P_{out} = qVocFF\int_{0}^{\infty} \bar{n}(\omega,T)e(\omega)EQE(\omega)d\omega \tag{3.13}$$

where q is the electronic charge, V_{OC} is open-circuit voltage, FF is fill-factor and EQE is the external quantum efficiency of used TPV cell, the term $\bar{n}(\omega,T)$ describes the density of incident photons given by [83]:

$$\bar{n}(\omega,T) = \frac{\omega^2}{4\pi^2 c^2}\frac{\hbar\omega}{(e^{\hbar\omega/KT}-1)} \tag{3.14}$$

The conversion efficiency η_{TPV} is defined as the product of the diode efficiency (η_{diode}), which is the power conversion efficiency of absorbed photons, and the spectral efficiency (η_{sp}). Since a TPV device involves these two components, its total efficiency is the product of these two components as shown in equation (3.15) [83]. Thus:

$$\eta_{TPV} = \eta_{sp}\eta_{diode} = \frac{P_{abs}}{P_{rad}}\frac{P_{out}}{P_{abs}} = \frac{VocI_{SC}FF}{P_{rad}} \tag{3.15}$$

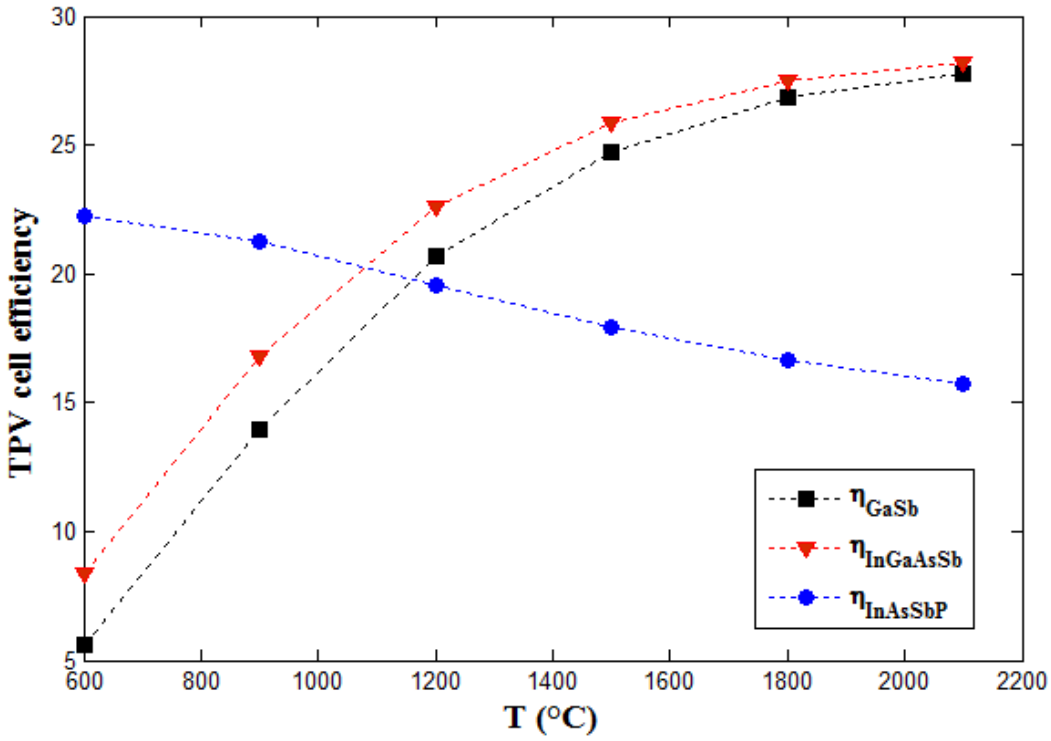

Figure 3. 8 : Comparison of T_{BB} dependent TPV conversion efficiency for the different TPV cells (GaSb, InGaAsSb, InAsSbP)

figure 3.8 shows the comparison of calculated TPV conversion efficiency for each cell at different temperatures, under low temperature (T_{BB} = 600ºC) less heat energy loss occurs, as it shows 22.5% conversion efficiency for InAsSbP, and both of GaSb and InGaAsSb at extremity does not surpasses 7%, on the other hand, for high temperature (1900-2100 ºC) TPV cell efficiency achieve 27% It shows much higher performance than InAsSbP, Therefore, the proposed absorber/emitter can operate at a wide temperature range from 600 to 2100 ºC.

3.4. Conclusion

A numerically computed design has been simulated by (HFSS) solver based on (FEM) approach, the outcome simulation confirmed by an experimental study reported by Sakurai et al from Niigata University (Japan 2019), we conclude that the absorption shows a good agreement with the experimental and simulation. this study shows that we have a new design of intermediate thin and compact film structures, with broadband absorption, polarization-insensitive, adequate for wide incident angles, and high melting temperature. Finally, our results exhibit a good TPV conversion efficiency of 27%, for commonly expelled PV cells.

Overall conclusion

The work contained in this manuscript started by studying and modeling a variety of TPV technologies. The key components for an efficient TPV system are the intermediate selective emitter and the high-quality choice of TPV cells. Making headway to explain and discuss the definition of the research field concerning Metamaterials (MTMs). Our choice of MTM emitter/absorber operating at visible and near-infrared frequencies, based on a new design suggested by the Japan research team (2019), the optical behavior of the structure is modeled using numerical solutions which use (FEM) method by (HFSS). The suggested absorber/emitter design together with three low-gap TPV cells (GaSb, InGaAsSb, InAsSbP), and scores a remarkable TPV conversion efficiency up to 27% at a temperature range of (1900-2100°C) for both GaSb and InGaAsSb, meanwhile, InAsSbP performed better at a low-temperature (600°C) more than 22%. In conclusion, it is evident that this study has shown that the suggested TPV system can operate efficiently at a wide temperature range from 600 to 2100 ºC, and revealed that they may operate at high and modest (wasted heat) temperatures all at one system. Our future work will be focused on the combination of the three TPV cells into a single tandem cell structure to absorb and convert all incidents waves for the largest working temperature range as possible.

Bibliography

[1] T. Bauer, *Thermophotovoltaics: Basic Principles and Critical Aspects of System Design*. Berlin, Heidelberg: Springer Berlin Heidelberg, 2011.

[2] C. Ferrari, F. Melino, M. Pinelli, P. R. Spina, et M. Venturini, « Overview and Status of Thermophotovoltaic Systems », *Energy Procedia*, vol. 45, p. 160‑169, janv. 2014, doi: 10.1016/j.egypro.2014.01.018.

[3] G. Colangelo, A. de Risi, et D. Laforgia, « New approaches to the design of the combustion system for thermophotovoltaic applications », *Semicond. Sci. Technol.*, vol. 18, n° 5, p. S262‑S269, mai 2003, doi: 10.1088/0268-1242/18/5/318.

[4] G. Mattarolo, *Development and modelling of a thermophotovoltaic system*. Kassel: Kassel Univ. Press, 2007.

[5] T. J. Coutts, « A review of progress in thermophotovoltaic generation of electricityfnafnaI began writing this paper immediately after the Third nrel Conference on Thermophotovoltaic Genertion of materials, devices, and systems; substantial gains in fundamental understanding and performance of the quaternary alloy GaInAsSb; the introduction of new radiator concepts; and more attention being paid to modeling of both real and conceptual systems. There was also further evidence of interest in non-military applications, particularly from the European and Japanese attendees. », *Renew. Sustain. Energy Rev.*, vol. 3, n° 2, p. 77‑184, juin 1999, doi: 10.1016/S1364-0321(98)00021-5.

[6] M. Herrando et C. N. Markides, « Hybrid PV and solar-thermal systems for domestic heat and power provision in the UK: Techno-economic considerations », *Appl. Energy*, vol. 161, p. 512‑532, janv. 2016, doi: 10.1016/j.apenergy.2015.09.025.

[7] F. Bendelala, « Modeling and performances optimization of thermophotovoltaic cells based on new metamaterials ».

[8] D. Wilt, D. Chubb, D. Wolford, P. Magari, et C. Crowley, « Thermophotovoltaics for Space Power Applications », in *AIP Conference Proceedings*, Madrid (Spain), 2007, vol. 890, p. 335‑345, doi: 10.1063/1.2711751.

[9] L. Broman et J. Marks, « Co-generation of electricity and heat from combustion of wood powder utilizing thermophotovoltaic conversion », in *AIP Conference Proceedings*, Copper Mountain, Colorado (USA), 1995, vol. 321, p. 133‑138, doi: 10.1063/1.47062.

[10] A. S. Vlasov, V. P. Khvostikov, O. A. Khvostikova, P. Y. Gazaryan, S. V. Sorokina, et V. M. Andreev, « TPV Systems with Solar Powered Tungsten Emitters », in *AIP Conference Proceedings*, Madrid (Spain), 2007, vol. 890, p. 327‑334, doi: 10.1063/1.2711750.

[11] P. A. Jurczak, « Development of III-V Semiconductor Materials for Thermophotovoltaic Cells », p. 197.

[12] G. Beghi, Éd., *Performance of Solar Energy Converters: Thermal Collectors and Photovoltaic Cells*. Dordrecht: Springer Netherlands, 1983.

[13] G. Mattarolo, *Development and modelling of a thermophotovoltaic system*. Kassel: Kassel Univ. Press, 2007.

[14] P. M. Fourspring, « Thermophotovoltaic Spectral Control », in *AIP Conference Proceedings*, Freiburg (Germany), 2004, vol. 738, p. 171‑179, doi: 10.1063/1.1841892.

[15] « TPV Systems — From Research Towards Commercialisation: AIP Conference Proceedings: Vol 738, No 1 ». https://aip.scitation.org/doi/10.1063/1.1841877 (consulté le mai 02, 2020).

[16] W. E. Horne, M. D. Morgan, V. S. Sundaram, et T. Butcher, « 500 Watt Diesel Fueled TPV Portable Power Supply », *AIP Conf. Proc.*, vol. 653, nº 1, p. 91‑100, janv. 2003, doi: 10.1063/1.1539367.

[17] W. R. Chan, V. Stelmakh, C. M. Waits, M. Soljacic, J. D. Joannopoulos, et I. Celanovic, « Photonic Crystal Enabled Thermophotovoltaics for a Portable Microgenerator », *J. Phys. Conf. Ser.*, vol. 660, p. 012069, déc. 2015, doi: 10.1088/1742-6596/660/1/012069.

[18] H. Sai, T. Kamikawa, Y. Kanamori, K. Hane, H. Yugami, et M. Yamaguchi, « Thermophotovoltaic Generation with Microstructured Tungsten Selective Emitters », *AIP Conf. Proc.*, vol. 738, nº 1, p. 206‑214, nov. 2004, doi: 10.1063/1.1841896.

[19] M. G. Mauk, O. Sulima, J. A. Cox, et R. L. Mueller, « Low-bandgap (0.3 to 0.5 eV) InAsSbP thermophotovoltaics: Assessment for open-circuit voltage improvements », juin 2003, p. 224-227 Vol.1, doi: 10.1109/WCPEC.2003.1305262.

[20] L. Besra et M. Liu, « A review on fundamentals and applications of electrophoretic deposition (EPD) », *Prog. Mater. Sci.*, vol. 52, nº 1, p. 1‑61, janv. 2007, doi: 10.1016/j.pmatsci.2006.07.001.

[21] D. L. Chubb, *Fundamentals of thermophotovoltaic energy conversion*, 1st ed. Amsterdam, Netherlands ; Boston: Elsevier, 2007.

[22] J. A. Kilner, S. J. Skinner, S. J. C. Irvine, et P. P. Edwards, *Functional Materials for Sustainable Energy Applications*. Elsevier Science, 2012.

[23] Z. Utlu et B. S. Önal, « Thermodynamic analysis of thermophotovoltaic systems used in waste heat recovery systems: an application », *Int. J. Low-Carbon Technol.*, vol. 13, nº 1, p. 52‑60, mars 2018, doi: 10.1093/ijlct/ctx019.

[24] D. M. Wilt, « Buffer Layer Effects on Tandem InGaAs TPV Devices », in *AIP Conference Proceedings*, Freiburg (Germany), 2004, vol. 738, p. 453‑461, doi: 10.1063/1.1841924.

[25] L. B. Karlina, A. S. Vlasov, M. M. Kulagina, et N. Kh. Timoshina, « Thermophotovoltaic cells based on In0.53Ga0.47As/InP heterostructures », *Semiconductors*, vol. 40, nº 3, p. 346‑350, mars 2006, doi: 10.1134/S1063782606030171.

[26] V. S. Sundaram *et al.*, « GaSb based ternary and quaternary diffused junction devices for TPV applications », in *Third NREL Conference on thermophotovoltaic generation of electricity*, Colorado Springs, Colorado (USA), 1997, p. 105‑115, doi: 10.1063/1.53277.

[27] O. V. Sulima, R. Beckert, A. W. Bett, J. A. Cox, et M. G. Mauk, « InGaAsSb photovoltaic cells with enhanced open-circuit voltage », *IEE Proc. - Optoelectron.*, vol. 147, nº 3, p. 199‑204, juin 2000, doi: 10.1049/ip-opt:20000500.

[28] A. W. Bett et O. V. Sulima, « GaSb photovoltaic cells for applications in TPV generators », *Semicond. Sci. Technol.*, vol. 18, nº 5, p. S184‑S190, mai 2003, doi: 10.1088/0268-1242/18/5/307.

[29] V. M. Andreev, « Low-Bandgap Ge and InAsSbP/InAs-Based TPV Cells », in *AIP Conference Proceedings*, Rome (Italy), 2003, vol. 653, p. 383‑391, doi: 10.1063/1.1539393.

[30] P. S. Dutta, « GaSb and Ga1−xInxSb Thermophotovoltaic Cells using Diffused Junction Technology in Bulk Substrates », in *AIP Conference Proceedings*, Rome (Italy), 2003, vol. 653, p. 392‑401, doi: 10.1063/1.1539394.

[31] V. Khvostikov *et al.*, « Thermophotovoltaic Cells Based on Low-Bandgap Compounds », vol. 738, nov. 2004, doi: 10.1063/1.1841922.

[32] M. W. Dashiell *et al.*, « Quaternary InGaAsSb Thermophotovoltaic Diodes », *IEEE Trans. Electron Devices*, vol. 53, nº 12, p. 2879‑2891, déc. 2006, doi: 10.1109/TED.2006.885087.

[33] M. K. Hudait, M. Brenner, et S. A. Ringel, « Metamorphic In0.7Al0.3As/In0.69Ga0.31As thermophotovoltaic devices grown on graded InAsyP1−y buffers by molecular beam epitaxy », *Solid-State Electron.*, vol. 53, nº 1, p. 102‑106, janv. 2009, doi: 10.1016/j.sse.2008.10.007.

[34] K. J. Cheetham, P. J. Carrington, N. B. Cook, et A. Krier, « Low bandgap GaInAsSbP pentanary thermophotovoltaic diodes », *Sol. Energy Mater. Sol. Cells*, vol. 95, nº 2, p. 534‑537, févr. 2011, doi: 10.1016/j.solmat.2010.08.036.

[35] R. S. Tuley, J. M. S. Orr, R. J. Nicholas, D. C. Rogers, P. J. Cannard, et S. Dosanjh, « Lattice-matched InGaAs on InP thermophovoltaic cells », *Semicond. Sci. Technol.*, vol. 28, nº 1, p. 015013, janv. 2013, doi: 10.1088/0268-1242/28/1/015013.

[36] Y.-Y. Lou, X.-L. Zhang, A.-B. Huang, et Y. Wang, « Enhanced thermal radiation conversion in a GaSb/GaInAsSb tandem thermophotovoltaic cell », *Sol. Energy Mater. Sol. Cells*, vol. 172, p. 124‑132, déc. 2017, doi: 10.1016/j.solmat.2017.07.030.

[37] Q. Lu, R. Beanland, D. Montesdeoca, P. J. Carrington, A. Marshall, et A. Krier, « Low bandgap GaInAsSb thermophotovoltaic cells on GaAs substrate with advanced metamorphic buffer layer », *Sol. Energy Mater. Sol. Cells*, vol. 191, p. 406‑412, mars 2019, doi: 10.1016/j.solmat.2018.11.036.

[38] M. P. Bernardi, O. Dupré, E. Blandre, P.-O. Chapuis, R. Vaillon, et M. Francoeur, « Impacts of propagating, frustrated and surface modes on radiative, electrical and

thermal losses in nanoscale-gap thermophotovoltaic power generators », *Sci. Rep.*, vol. 5, nº 1, p. 11626, déc. 2015, doi: 10.1038/srep11626.

[39] D. R. Smith, W. J. Padilla, D. C. Vier, S. C. Nemat-Nasser, et S. Schultz, « Composite Medium with Simultaneously Negative Permeability and Permittivity », *Phys. Rev. Lett.*, vol. 84, nº 18, p. 4184‑4187, mai 2000, doi: 10.1103/PhysRevLett.84.4184.

[40] J. C. Bose, « On the Rotation of Plane of Polarisation of Electric Waves by a Twisted Structure », *Proc. R. Soc. Lond.*, vol. 6, p. 146‑152, 1898.

[41] C. G. Christodoulou et P. F. Wahid, *Fundamentals of Antennas: Concepts and Applications*. SPIE Press, 2001.

[42] J. Brown, « ARTIFICIAL DIELECTRICS HAVING REFRACTIVE INDICES LESS THAN UNITY », p. 12.

[43] V. G. Veselago, « THE ELECTRODYNAMICS OF SUBSTANCES WITH SIMULTANEOUSLY NEGATIVE VALUES OF ϵ AND μ », *Sov. Phys. Uspekhi*, vol. 10, nº 4, p. 509‑514.

[44] J. B. Pendry, « Negative Refraction Makes a Perfect Lens », *Phys. Rev. Lett.*, vol. 85, nº 18, p. 3966‑3969, oct. 2000, doi: 10.1103/PhysRevLett.85.3966.

[45] W. J. Padilla, D. N. Basov, et D. R. Smith, « Negative refractive index metamaterials », *Mater. Today*, vol. 9, nº 7, p. 28‑35, juill. 2006, doi: 10.1016/S1369-7021(06)71573-5.

[46] N. Engheta et R. W. Ziolkowski, « Physics and Engineering Explorations », p. 438.

[47] P. Moitra, Y. Yang, Z. Anderson, I. I. Kravchenko, D. P. Briggs, et J. Valentine, « Realization of an all-dielectric zero-index optical metamaterial », *Nat. Photonics*, vol. 7, nº 10, p. 791‑795, oct. 2013, doi: 10.1038/nphoton.2013.214.

[48] « THE SIMULATION AND STRUCTURE DESIGN OF OPTICAL METAMATERIALS | Research Explorer | The University of Manchester ». https://www.research.manchester.ac.uk/portal/en/theses/the-simulation-and-structure-design-of-optical-metamaterials(b85aac76-61cf-4269-864a-5c0de60b715a).html (consulté le août 13, 2020).

[49] K. Diest, Éd., *Numerical Methods for Metamaterial Design*, vol. 127. Dordrecht: Springer Netherlands, 2013.

[50] W. Cai et V. Shalaev, *Optical Metamaterials*. New York, NY: Springer New York, 2010.

[51] A. Freise, « Optical Metamaterials: Fundamentals and Applications, by W. Cai and V. Shalaev », *Contemp. Phys.*, vol. 53, nº 3, p. 278‑279, mai 2012, doi: 10.1080/00107514.2012.661780.

[52] W. M. Telford, W. M. Telford, L. P. Geldart, R. E. Sheriff, et R. E. Sheriff, *Applied Geophysics*. Cambridge University Press, 1990.

[53] X. C. Tong, *Functional Metamaterials and Metadevices*, vol. 262. Cham: Springer International Publishing, 2018.

[54] A. Zagoskin, D. Felbacq, et E. Rousseau, « Quantum metamaterials in the microwave and optical ranges », *EPJ Quantum Technol.*, vol. 3, déc. 2016, doi: 10.1140/epjqt/s40507-016-0040-x.

[55] A. M. Zagoskin, D. Felbacq, et E. Rousseau, « Quantum metamaterials in the microwave and optical ranges », *EPJ Quantum Technol.*, vol. 3, nº 1, p. 2, févr. 2016, doi: 10.1140/epjqt/s40507-016-0040-x.

[56] S. Choudhury *et al.*, « Material platforms for optical metasurfaces », *Nanophotonics*, vol. 7, mai 2018, doi: 10.1515/nanoph-2017-0130.

[57] X. Luo, M. Pu, X. Ma, et X. Li, « Taming the Electromagnetic Boundaries via Metasurfaces: From Theory and Fabrication to Functional Devices », *International Journal of Antennas and Propagation*, oct. 04, 2015. https://www.hindawi.com/journals/ijap/2015/204127/ (consulté le août 13, 2020).

[58] B. Luk'yanchuk *et al.*, « The Fano resonance in plasmonic nanostructures and metamaterials », *Nat. Mater.*, vol. 9, p. 707‑15, sept. 2010, doi: 10.1038/nmat2810.

[59] « Plasmon », *Wikipedia*. juin 18, 2020, Consulté le: août 13, 2020. [En ligne]. Disponible sur: https://en.wikipedia.org/w/index.php?title=Plasmon&oldid=963226733.

[60] N. yu *et al.*, « Light Propagation with Phase Discontinuities: Generalized Laws of Reflection and Refraction », *Science*, vol. 334, p. 333‑7, sept. 2011, doi: 10.1126/science.1210713.

[61] X. Ni, N. K. Emani, A. V. Kildishev, A. Boltasseva, et V. M. Shalaev, « Broadband Light Bending with Plasmonic Nanoantennas », *Science*, vol. 335, nº 6067, p. 427‑427, janv. 2012, doi: 10.1126/science.1214686.

[62] J. Khurgin, « How to deal with the loss in plasmonics and metamaterials », *Nat. Nanotechnol.*, vol. 10, p. 2‑6, janv. 2015, doi: 10.1038/nnano.2014.310.

[63] P. Genevet, F. Capasso, F. Aieta, M. Khorasaninejad, et R. Devlin, « Recent advances in planar optics: From plasmonic to dielectric metasurfaces », *Optica*, vol. 4, p. 139, janv. 2017, doi: 10.1364/OPTICA.4.000139.

[64] A. I. Kuznetsov, A. E. Miroshnichenko, M. L. Brongersma, Y. S. Kivshar, et B. Luk'yanchuk, « Optically resonant dielectric nanostructures », *Science*, vol. 354, nº 6314, p. aag2472, nov. 2016, doi: 10.1126/science.aag2472.

[65] « (PDF) Experimental demonstration of a broadband all-dielectric metamaterial perfect reflector ». https://www.researchgate.net/publication/262025919_Experimental_demonstration_of_a_broadband_all-dielectric_metamaterial_perfect_reflector (consulté le juill. 02, 2020).

[66] P. Moitra *et al.*, « Large-Scale All-Dielectric Metamaterial Perfect Reflectors », *ACS Photonics*, vol. 2, mai 2015, doi: 10.1021/acsphotonics.5b00148.

[67] R. Sakakibara *et al.*, « Practical emitters for thermophotovoltaics: a review », *J. Photonics Energy*, vol. 9, nº 3, p. 032713, févr. 2019, doi: 10.1117/1.JPE.9.032713.

[68] A. Bossavit, *Computational Electromagnetism: Variational Formulations, Complementarity, Edge Elements*. Academic Press, 1998.

[69] « Engineering Simulation & 3D Design Software | Ansys ». https://www.ansys.com/ (consulté le juill. 23, 2020).

[70] *R. Courant, ―Variational methods for the solution of problems of equilibrium and vibrations,‖ Bull. Amer. Math. Soc., vol. 49, no. 1, pp. 1–23, Jan. 1943. .*

[71] S. Ahmed et P. Daly, « Finite-element methods for inhomogeneous waveguides », *Proc. Inst. Electr. Eng.*, vol. 116, nº 10, p. 1661‑1664, oct. 1969, doi: 10.1049/piee.1969.0300.

[72] E. Nefzaoui, J. Drevillon, et K. Joulain, « Selective emitters design and optimization for thermophotovoltaic applications », *J. Appl. Phys.*, vol. 111, nº 8, p. 084316, avr. 2012, doi: 10.1063/1.4705363.

[73] A. Sakurai et Y. Matsuno, « Design and Fabrication of a Wavelength-Selective Near-Infrared Metasurface Emitter for a Thermophotovoltaic System », *Micromachines*, vol. 10, nº 2, p. 157, févr. 2019, doi: 10.3390/mi10020157.

[74] F. Bendelala, A. Cheknane, et H. S. Hilal, « A broad-band polarization-insensitive absorber with a wide angle range metamaterial for thermo-photovoltaic conversion », *Opt. Quantum Electron.*, vol. 50, nº 1, p. 10, déc. 2017, doi: 10.1007/s11082-017-1273-3.

[75] M. A. Ordal *et al.*, « Optical properties of the metals Al, Co, Cu, Au, Fe, Pb, Ni, Pd, Pt, Ag, Ti, and W in the infrared and far infrared », *Appl. Opt.*, vol. 22, nº 7, p. 1099‑1119, avr. 1983, doi: 10.1364/AO.22.001099.

[76] E. D. Palik, *Handbook of Optical Constants of Solids*. Academic Press, 1998.

[77] B. J. Lee, L. P. Wang, et Z. M. Zhang, « Coherent thermal emission by excitation of magnetic polaritons between periodic strips and a metallic film », *Opt. Express*, vol. 16, nº 15, p. 11328‑11336, juill. 2008, doi: 10.1364/OE.16.011328.

[78] B. Zhao, L. Wang, Y. Shuai, et Z. M. Zhang, « Thermophotovoltaic emitters based on a two-dimensional grating/thin-film nanostructure », *Int. J. Heat Mass Transf.*, vol. 67, p. 637‑645, déc. 2013, doi: 10.1016/j.ijheatmasstransfer.2013.08.047.

[79] B. Wang, T. Koschny, et C. M. Soukoulis, « Wide-angle and polarization-independent chiral metamaterial absorber », *Phys. Rev. B*, vol. 80, nº 3, p. 033108, juill. 2009, doi: 10.1103/PhysRevB.80.033108.

[80] B. Zhu, Z. Wang, C. Huang, Y. Feng, J. Zhao, et T. Jiang, « Polarization Insensitive Metamaterial Absorber with Wide Incident Angle », *Prog. Electromagn. Res.*, vol. 101, p. 231‑239, 2010, doi: 10.2528/PIER10011110.

[81] O. V. Sulima, A. W. Bett, M. G. Mauk, F. Dimroth, P. S. Dutta, et R. L. Mueller, « GaSb-, InGaAsSb-, InGaSb-, InAsSbP- and Ge-TPV cells for low-temperature TPV applications », *AIP Conf. Proc.*, vol. 653, n° 1, p. 434‑441, janv. 2003, doi: 10.1063/1.1539398.

[82] A. Salim et S. Lim, « Review of Recent Metamaterial Microfluidic Sensors », *Sensors*, vol. 18, n° 1, Art. n° 1, janv. 2018, doi: 10.3390/s18010232.

[83] F. Bendelala, A. Cheknane, et H. Hilal, « Enhanced low-gap thermophotovoltaic cell efficiency for a wide temperature range based on a selective meta-material emitter », *Sol. Energy*, vol. 174, p. 1053‑1057, nov. 2018, doi: 10.1016/j.solener.2018.10.006.